Ertel potential vorticity versus Bernoulli streamfunction on Mars

T. E. Dowling, [a]* M. E. Bradley,[b] J. Du,[a] S. R. Lewis[c] and P. L. Read[d]

[a] *Department of Physics & Astronomy, University of Louisville, Kentucky 40292, USA*
[b] *Department of Mathematics, University of Louisville, Kentucky 40292, USA*
[c] *Department of Physical Sciences, The Open University, Milton Keynes MK7 6AA, UK*
[d] *Atmospheric, Oceanic and Planetary Physics, University of Oxford OX1 3PU, UK*

*Correspondence to: T. E. Dowling, Dept. of Physics & Astronomy, University of Louisville, Kentucky 40292 USA.
E-mail: dowling@louisville.edu

Scatter plots of Ertel potential vorticity, Q, versus Bernoulli streamfunction, B, on potential-temperature surfaces, θ, are investigated for Mars using the global Mars Analysis Correction Data Assimilation (MACDA) reanalysis, which spans Mars Year (MY) 24.39 to 27.24. In mid-latitudes, Mars exhibits monotonic, function-like $Q(B)$ correlations on θ surfaces similar to those observed for Earth. We quantify this with linear regressions of Q versus B over the vertical range $\theta = 400$ to $900\,\mathrm{K}$ (∼30 to 60 km). In autumn, winter and spring, in both hemispheres, the nondimensionalized correlation generally lies between zero and unity and gradually decreases with height, whereas in northern summer, it swings negative. These characteristics match Earth's lower mesosphere ($\theta = 2000$ to $3000\,\mathrm{K}$; $z \approx 48$ to $62\,\mathrm{km}$) during the same seasons. The exception is southern summer, when the correlation on Mars nearly vanishes. In time series, the transition into and out of northern summer is sinuous and centred just after solar longitude $L_s = 90°$, whereas in southern summer it is abrupt and spans $\Delta L_s \approx 120°$, which is 1/3 of a Mars year. A striking feature seen on Mars but not on Earth is a large range of Q over the narrow domain of B poleward of each winter polar jet, particularly in the north, which is consistent with the known annular structure for the Martian polar vortex. Froude number calculations suggest the existence of a planetary-scale hydraulic jump associated with the winter polar jet.

Key Words: Mars; martian atmosphere; middle atmosphere

Received . . .

1. Introduction

Correlations between vorticity and streamfunction provide a well-established means of characterizing both steady and unsteady geophysical fluid systems, including free modes (*Read et al.* 1986; *Marshall and So* 1990), basic states (*White* 1990), the vertical propagation of Rossby-waves, starting with the classic work of *Charney and Drazin* (1961), and shear stability (*Read et al.* 2006, 2009a,b). Traditionally, this type of analysis has been carried out in the rapid rotation, strong stratification quasi-geostrophic limit, but efforts have been made recently to focus on primitive-equation variables for which the only strong assumption is hydrostatic balance, including a recent application to Earth's extra-tropical atmosphere by *Du et al.* (2015, hereafter DDB). The goal of this article is to apply a similar analysis to Mars.

1.1. Primitive variables

For hydrostatic, isentropic flow, in the steady limit, momentum and mass conservation combine to yield the primitive-variable relationship

$$Q = \frac{dB}{d\Psi}\,, \tag{1}$$

(e.g. *Gill* 1982, pp. 231–233; *Vallis* 2006, pp. 190–192; *Schär* 1993) where Q is the Ertel potential vorticity (PV), which in the hydrostatic limit may be written

$$Q = \frac{\zeta + f}{\tilde{h}}\,, \tag{2}$$

f is the Coriolis parameter (planetary vorticity), ζ is the relative vorticity computed on potential-temperature surfaces, θ,

$$\tilde{h} = -\frac{1}{g}\frac{\partial p}{\partial \theta} \tag{3}$$

is the thickness density (*Vallis* 2006, p. 225), g is the gravity and p is the pressure. The Bernoulli streamfunction, or specific total dry energy, is

$$B = \phi + h + K\,, \tag{4}$$

where ϕ is the geopotential, h (not to be confused with $\tilde{h}$) is the specific enthalpy and K is the specific horizontal kinetic energy.

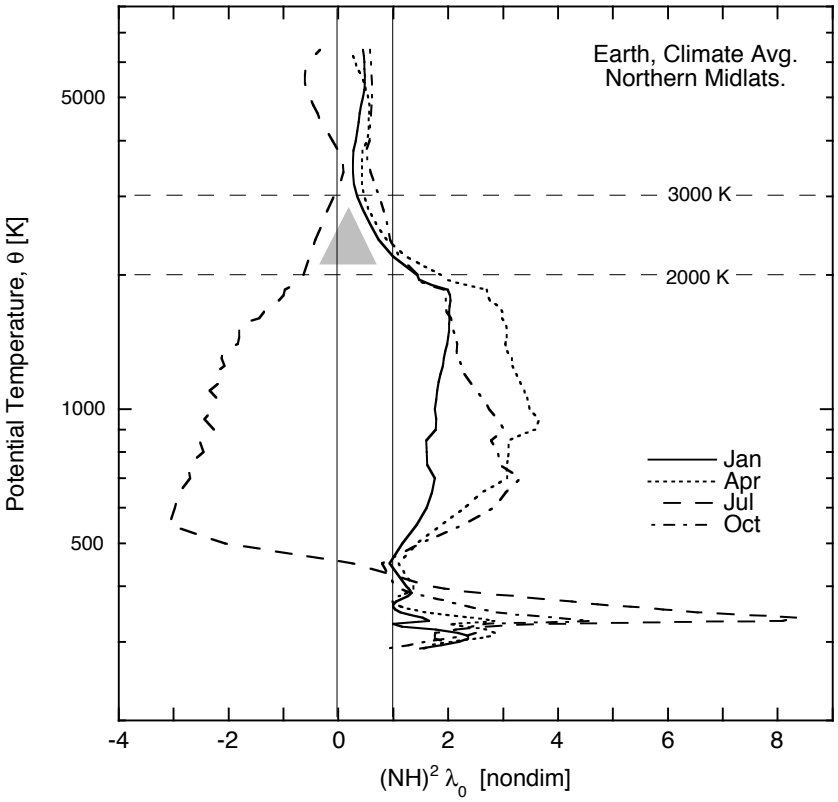

Figure 1. Vertical profiles of the correlation between Ertel potential vorticity (Q or PV), and Bernoulli streamfunction, B, for Earth's northern mid-latitudes. Shown is the nondimensional parameter, $\hat{\lambda}_0 \equiv \overline{(NH)^2}\lambda_0$, corresponding to the exponential $Q(B)$ model (7a), versus potential temperature, θ, the vertical coordinate in this analysis. The profiles are the monthly climate averages (1979–2009) of λ_0 calculated by DDB, for January, April, July and October, over the 30° to 60° latitude region, multiplied by $\overline{(NH)^2}$ based on the U.S. Standard Atmosphere. The positive spikes in $\hat{\lambda}_0$ at the bottom occupy the troposphere. The stratopause is at $\theta \approx 2000$ K and the mesopause is at $\theta \approx 10{,}000$ K (not shown). The shaded triangle highlights the lower mesosphere, in which $|\hat{\lambda}_0|$ starts near unity and decreases with altitude.

The horizontal, mass-weighted streamfunction, Ψ, in the steady-state case satisfies

$$\tilde{h}u = -\frac{\partial \Psi}{\partial y}\Big|_\theta, \quad \tilde{h}v = \frac{\partial \Psi}{\partial x}\Big|_\theta, \tag{5}$$

where x and y are the local-cartesian zonal (eastward) and meridional (northward) coordinates, and u and v are the zonal and meridional components of the velocity.

It has been known for decades that in Earth's unsteady atmosphere, the above primitive-variable versions of potential vorticity and streamfunction have correlations on θ surfaces that are approximately function-like with some scatter (*White* 1990). Under such conditions, one may pick whichever of the three pairings, $Q(\Psi)$, $Q(B)$, or $B(\Psi)$, is most convenient to investigate, because the others follow upon integration of (1), written either as $dB = Qd\Psi$ or $d\Psi = Q^{-1}dB$; two examples are shown below. Following DDB, we focus on $Q(B)$, since B is a sum of terms in hand, whereas calculation of Ψ involves inverting an elliptic operator.

1.2. *Earth*

For Earth's extra-tropical atmosphere, DDB show that Q versus B scatter plots are well correlated, even in snapshots, and that the correlation parameter, $\lambda_0 = -d\log|Q|/dB$, distinguishes between the troposphere, stratosphere and mesosphere. *Dowling* (2014) introduced a nondimensional version, $\hat{\lambda}_0 = \overline{(NH)^2}\lambda_0$, where N is the buoyancy frequency, H is the pressure scale height, and their product is squared and averaged over the region in question.

Figure 1 shows profiles of $\hat{\lambda}_0$ versus θ for Earth's northern mid-latitude region, based on DDB's monthly climate averages. The positive spikes at the bottom occupy the troposphere. Both the stratosphere's lower end and upper end, the stratopause ($\theta \approx 2000\,\mathrm{K}$), are characterized by $\hat{\lambda}_0 \approx 1$. Summer is marked by negative correlations in the middle atmosphere (the dashed curve is July), which are associated with Earth's seasonal zonal-wind reversal.

1.3. *Vertical range*

Mars does not have a stratosphere in which temperature generally increases with height (*Read et al.* 2015). In this study, we focus on the altitude range ∼30 to ∼60 km, which lies well above the convective planetary boundary layer and mountains, and well below the top of the Mars General Circulation Model (Mars-GCM) used in the reanalysis described in the next section. The bottom third of this range is constrained by remote sensing, whereas its top two-thirds come from modeling alone. The pressures in terms of actual values line up with Earth's mesosphere. For later reference, Earth's lower mesosphere is highlighted in Fig. 1 by the shaded triangle—this is where the Mars profiles from this work match Earth's atmosphere.

Our vertical coordinate is potential temperature, θ, which is related to specific entropy, s, via $ds = c_p\, d\log\theta$, where c_p is the specific heat capacity at constant pressure. Mars studies to date have usually employed altitude or pressure as the vertical coordinate, not potential temperature. An air parcel on Mars has a relatively short radiative relaxation timescale, on the order of a day, compared to weeks on Earth. If J denotes the specific diabatic heating rate, and t denotes time, then the analogue of vertical velocity in θ coordinates is $d\theta/dt \equiv \dot{\theta} = J/\Pi$, where $\Pi \equiv c_pT/\theta$ is the Exner function. Since $\dot{\theta}$ is not small when J is appreciable, the system is not rendered quasi-horizontal in θ coordinates. However, this is about all one loses for Mars—there remain fundamental reasons to proceed related to potential-vorticity invertibility (*Hoskins et al.* 1985).

We calculate θ via the standard Poisson power law, $\theta(p,T) = T(p_0/p)^\kappa$, where $\kappa = R_d/c_p$ is the Poisson exponent, R_d is the dry-air gas constant, p_0 is a reference pressure, and c_p is a reference specific heat (*Holton and Hakim* 2013). A commonly used reference surface pressure on Mars is $6.1\,\mathrm{hPa} = 610\,\mathrm{Pa}$, which we adopt for p_0, such that $\theta \approx T$ near the surface. This means θ takes on different values between the planets at a given p and T, because $p_0 = 1000\,\mathrm{hPa}$ for Earth—the rule of thumb is θ on Mars is roughly a factor of 4 less than θ on Earth. The ratio, $\theta_{\mathrm{Mars}}/\theta_{\mathrm{Earth}} < 1$, changes with pressure because κ is significantly different between the planets. The dry gas constant, R_d, does not change appreciably with altitude or temperature on Mars; the standard value, which we use, is $R_d = 192\,\mathrm{Jkg^{-1}K^{-1}}$ (*Zurek et al.* 1992, Table I, p. 855). Physical temperatures in this study range from $T \sim 130$ to $220\,\mathrm{K}$, for which $c_p(T)$ varies by 12% (*Woolley* 1954). Here we set $c_p = 735\,\mathrm{Jkg^{-1}K^{-1}}$, which is the value at $T \approx 200\,\mathrm{K}$. This value is used in other Mars GCMs (e.g. *Urata and Toon* 2013; *R. Haberle* 2015, private communication) and yields the Poisson exponent, $\kappa = 0.261$.

The vertical span is set to be $\theta = 400$ to $900\,\mathrm{K}$, which corresponds to the aforementioned altitudes on average. We step through this range in $\Delta\theta = 25\,\mathrm{K}$ increments. To help orient the reader, below we show plots of zonally averaged geopotential height and pressure on representative θ surfaces (Figs. 2 and 3).

1.4. *Overview*

The rest of the paper is organized as follows. In section 2, we describe the prognostic, primitive-variable input data, which come in sigma coordinates (terrain following, $\sigma = p/p_{\mathrm{surf}}$), followed by the interpolation of these onto the potential temperature surfaces just delineated, then the calculation of Ertel PV and Bernoulli streamfunction. In section 3, we present isentropic-analysis results as a function of season, including scatter plots of Q versus B. In section 4, we present linear-regression best fits and compare quantitatively with DDB's results for Earth. In section 5, we summarize and make conclusions.

2. Input Data

2.1. *MACDA reanalysis*

The present study is made possible by the open release* of Version 1.0 of the Mars Analysis Correction Data Assimilation (MACDA) global reanalysis (*Montabone et al.* 2014). This reanalysis was created by assimilating nadir soundings from the NASA Mars Global Surveyor (MGS) Thermal Emission Spectrometer (TES) into the United Kingdom (UK) version of the Laboratoire de Météorologie Dynamique (LMD) Mars General Circulation Model (Mars-GCM), developed through a collaboration between groups in France (*Forget et al.* 1999) and the UK (*Lewis et al.* 1999).

For reference, one Mars day, or sol, is about 40 minutes longer than one Earth day, and one Mars year is about 687 Earth days. The MACDA V1.0 distribution is comprised of 63 self-describing netCDF† files, which span 30 sols each and include the following primitive variables, reported 12 times per sol: zonal wind, u, meridional wind, v, temperature, T, and pressure, p. The files also include variables not directly used in this study, such as dust optical thickness and CO_2 ice. The net result is a continuous global record starting in the middle of Mars Year (MY) 24 and ending in the middle of MY 27. This sampling period corresponds to 1999–2004, when MGS was in its science mapping phase (i.e. in a circular orbit, after its cruise and aerobraking phases). It includes a planet-encircling, or global, dust-storm in MY 25 (*Cantor* 2007), as well as a significant regional dust storm in MY 26 that peaked at solar longitude $L_s \sim 321^\circ$ (*Kass et al.* 2016) and coincided with an equatorward displacement of the polar vortex. *Mitchell et al.* (2015) found the latter storm shares some qualitative similarities with stratospheric sudden warmings (SSW) on Earth.

As alluded to above, the MGS/TES temperature retrievals provide observational constraints at and below about 40 km altitude (*Montabone et al.* 2014). This corresponds to approximately the bottom third of our vertical range. The MACDA data above this altitude are supplied by the Mars-GCM alone. This is not unlike the Canadian Middle Atmosphere Model (CMAM) reanalysis used by DDB, which is constrained by observations in Earth's troposphere and stratosphere, but in the mesosphere is supplied by the CMAM model alone.

2.2. *Conversion to isentropic coordinates*

The platform we use for the isentropic analysis is the Explicit Planetary Isentropic Coordinate (EPIC) atmospheric model (*Dowling et al.* 1998, 2006), which has been successfully employed in gas-giant atmospheric modeling for two decades.‡ An advantage of using EPIC is that it comes with subroutines needed to accurately calculate Q and B on θ surfaces. The MACDA variables are interpolated onto EPIC's staggered grids (C-grid scheme, *Arakawa and Lamb* 1977), which places the horizontal-wind components into a centred-difference stencil for the accurate calculation of PV.§ Each such interpolation is done via cubic splines (PCHIP, piecewise cubic Hermite interpolating polynomials; *Fritsch and Carlson* 1980) as follows.

2.2.1. *Interpolation*

In the vertical direction, MACDA variables are interpolated onto the EPIC θ surfaces in the same manner employed by DDB: to maintain monotonicity, points are excluded from the columnar source data table when the MACDA θ value is not larger than its value on the level below. We use 21 layers in EPIC to maintain similar resolution to the input data. In EPIC, pressure, p, is staggered vertically with respect to the winds.

In the meridional (latitude) direction, the V-grid and Q-grids are matched exactly, at the equator, to the original MACDA positions. There is extra latitude spacing at the poles for the V-grid and Q-grid (see Figs. 1 and 3 in *Dowling et al.* 1998), which provides consistency between the finite-difference continuity and vorticity equations on the sphere (*Arakawa and Lamb* 1981). This yields 36 latitude grid points for the V-grid and Q-grid in EPIC, including the two poles, and 35 grid points with uniform 4.94° spacing for the U-grid and H-grid¶, which do not have pole points. Before interpolating u onto the U-grid, we add pole values set to $u = 0$, and the same for v.

In the zonal (longitude) direction, for the U-grid we use the identical positions and 5° grid spacing as in the MACDA files, i.e. direct insertion, with $360^\circ/5^\circ = 72$ grid points. The V-grid and H-grid positions are staggered by one-half grid spacing. For this project we added a periodic version of the PCHIP spline to EPIC to facilitate zonal interpolations. All output variables are co-located (unstaggered) on the H-grid for convenience.

*The MACDA reanalysis is publicly available via registration with the British Atmospheric Data Centre (BADC).
†http://doi.org/10.5065/D6H70CW6

‡https://scholar.google.com/citations?user=6LJV7-UAAAAJ&hl=en
§The EPIC MACDA-processing mode can now be easily adapted to facilitate isentropic analysis of other primitive, prognostic-variable input files.
¶"H-grid" refers to the thickness density, $\tilde{h}$; its name is a holdover from shallow-water notation. In addition to $\tilde{h}$, this grid also carries the kinetic energy and divergence fields.

2.2.2. *Geopotential*

To calculate B we need the geopotential, ϕ, which in this primitive-equation context is obtained by integrating an appropriate form of the hydrostatic-balance equation up from the surface geopotential, ϕ_s. For this integration, EPIC uses the finite-difference algorithm (3.3) in *Konor and Arakawa* (1997). The MACDA V1.0 files do not include ϕ_s for Mars. EPIC does include this, but we discovered it is not in a form compatible with the MACDA reanalysis. Specifically, EPIC's ϕ_s for Mars is formed as a composite function, $\phi_s = \phi(\mathrm{lon}, \mathrm{lat}, \mathrm{r_s}(\mathrm{lon}, \mathrm{lat}))$, where the general geopotential, $\phi(\mathrm{lon}, \mathrm{lat}, \mathrm{r})$ is given by the Mars Reconnaissance Orbiter (MRO) 95^{th} degree and order gravity spherical-harmonic model (*Zuber* 2008, `jgmro_095a_sha`), and the planet's shape, or surface radius from its centre, $r_s(\mathrm{lon}, \mathrm{lat})$, is given by the Mars Orbiter Laser Altimeter (MOLA) 90^{th} degree and order model (`gtm090aa_sha`). However, these include the planet's rotational flattening[‖], and this is a problem because MACDA is based on the spectral version of the Mars-GCM, which assumes Mars is not rotationally flattened. We discovered this incompatibility when we noticed a large, systematic shift in our calculated geostrophic zonal wind, u_g, compared to the actual zonal wind, u.

For this project we remove the rotational flattening by reducing by 94% the spherical harmonic coefficient of degree 2 and order 0, $C_{20} \equiv J_2$, in the above $r_s(\mathrm{lon}, \mathrm{lat})$ model (*Wieczorek and Zuber* 2004), call it r'_s, and set $\phi_s = g_0[r'_s(\mathrm{lon}, \mathrm{lat}) - \mathrm{r}'_0]$, where $g_0 = 3.71\,\mathrm{ms}^{-2}$ is the standard reference value for the acceleration of gravity and r'_0 is the average at the equator. This makes the calculations of ϕ_s, ϕ and B in EPIC consistent with the MACDA reanalysis.

3. Isentropic Analysis

In what follows, MY 26 is treated as a baseline year, since: i) there does not yet exist a 30-planet-year climate average like for Earth and ii) MY 26 is complete in the MACDA data set and does not have a planet-encircling dust storm like MY 25.

3.1. *Z and p versus season*

Consider θ surfaces in terms of altitude and pressure as a function of season. Figure 2 shows the zonal average of geopotential height, $Z \equiv \phi/g_0$, versus latitude, for $\theta = 400$ to $900\,\mathrm{K}$ in $100\,\mathrm{K}$ steps, for the four canonical-season snapshots in MY 26, corresponding to the solar longitudes, $L_s = 0°$, $90°$, $180°$ and $270°$. For reference, the zonal average of surface topography, $Z_s \equiv \phi_s/g_0$, and the silhouette of highest topography are included. As advertised, the $\theta = 400\,\mathrm{K}$ surface stays well clear of the mountains in all seasons. Also shown are contours of zonal wind, u, which we zonally average in θ coordinates (consequently, the plotted contours of u are restricted to the θ range).

The two equinoxes are shown in the left panels in Fig. 2. They approximately exhibit mirror symmetry about the equator, with broad, flat tropical regions and smooth, tanh-like steps down to small, relatively flat polar regions. The two solstices are shown in the right panels. They exhibit a step in each winter hemisphere that is associated with the winter polar jet. The solstices on Mars are known to be quite different, in large measure because Mars has an elliptical orbit and perihelion falls on $L_s = 251°$, such that there is stronger thermal forcing in southern-summer / northern-winter, $L_s \sim 270°$. This results in a larger step associated with the northern-winter polar jet (right half of Fig. 2d), as well as a hypsometric flaring of the southern-summer layers (left half of Fig. 2d), which is not replicated in northern summer (right half of Fig. 2b). This flaring is associated with the homogenization of PV on Mars across essentially all of its southern hemisphere and half of its northern hemisphere at $L_s \sim 270°$, which is discussed below.

Figure 3 shows the seasonal variation of pressure on $\theta = 400$ to $900\,\mathrm{K}$ in MY 26. As expected, this and the previous plot are qualitatively similar. Earth has both a troposphere and a stratosphere positioned underneath its mesosphere, such that the altitude range of its mesosphere, $\sim 50\,\mathrm{km}$ at the stratopause to $\sim 85\,\mathrm{km}$ at the mesopause, if included in Fig. 2 would fall in the upper third of the plot. Nevertheless, the pressure range of Earth's mesosphere, $\sim 75\,\mathrm{Pa}$ to $\sim 0.35\,\mathrm{Pa}$, aligns with the martian study region in terms of actual pressure values.

3.2. *B and Q versus season*

3.2.1. *Bernoulli streamfunction*

Figure 4 shows the Bernoulli streamfunction, $B = \phi + c_pT + K$, versus latitude for the four canonical season points in MY 26, with the specific enthalpy approximated, at this point forward, by $h \approx c_pT$, where c_p is the reference value adopted above. An attribute that jumps out is that B is smoother than its components, including ϕ (Fig. 2), c_pT, which is proportional to p^κ on a θ surface and hence looks like p (Fig. 3), and K, which is dominated by the jets.

When interpreting the Q versus B scatter plots to follow, it is important to keep in mind that B is rather flat in the tropical region, and this plateau is broad during equinoxes, approximately $-40°$ to $+40°$ latitude. In each summer hemisphere, across the mid-latitudes, B increases poleward more-or-less monotonically and smoothly, such that it and the absolute value of latitude could be surrogates for one another. Across the winter-polar jet, B drops moving poleward, most strongly in northern winter ($L_s \sim 270°$), and then levels out.

3.2.2. *Potential vorticity*

To date, Mars studies have tended not to make extensive use of PV as a quasi-conserved quantity, owing in part to the relatively short radiative timescales, although in regions where diabatic heating is weaker and PV is conserved over longer periods, some studies have employed forms of it as a diagnostic, for example in studies of the polar vortices (*McConnochie* 2011; *Mitchell et al.* 2015). One stand out is *Barnes and Haberle* (1996), who used a Mars GCM to find that, during northern winter solstice conditions ($L_s \sim 270°$), the martian tropical and mid-latitude atmospheric circulation approximates to an angular-momentum conserving Hadley circulation, and is responsible for creating the broad region of low PV alluded to above.

In astrophysics, a synonym for PV is "vortensity", because it is a vorticity divided by a density, namely, absolute vorticity, $\zeta + f$, divided by thickness density, $\tilde{h}$ (2, 3). This denominator generates an exponential increase in Q with height, which, because Q is a signed quantity, requires some strategy besides a logarithm to manage. For this purpose, some authors plot Q multiplied by an average of its denominator on each θ surface, but we elect to transpose the organization and show the four seasons together on each θ surface.

Figure 5 shows the results. The shapes of the PV profiles for a given L_s are similar between θ surfaces, while the range of the ordinate grows rapidly with θ, as expected. Throughout the year, the profiles in Fig. 5 tend to be flatter with respect to latitude in the tropical region than across the mid-latitudes. This is similar to the flattening of B just mentioned, and consequently is muted in Q

[‖] The average equatorial and polar radii of Mars are 3396 and 3376 km, respectively, and the north pole is 6 km lower than the south pole (*Seidelmann et al.* 2007).

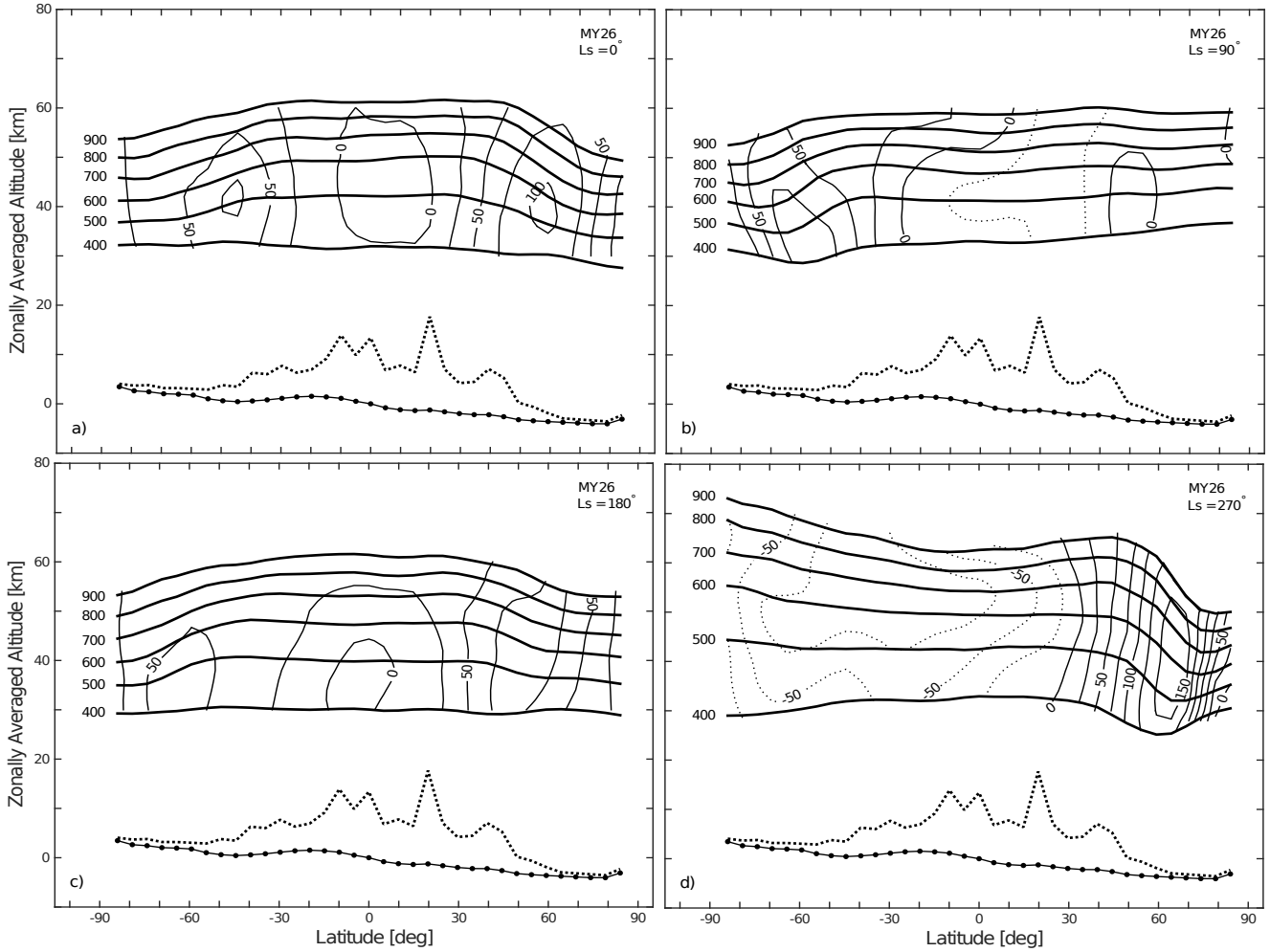

Figure 2. Geopotential height, $Z = \phi/g_0$, and zonal wind, u, versus latitude. Shown are snapshots from MY 26, at the northern a) vernal equinox, $L_s = 0^\circ$, b) summer solstice, $L_s = 90^\circ$, c) autumnal equinox, $L_s = 180^\circ$, and d) winter solstice, $L_s = 270^\circ$. The variables are zonally averaged in θ coordinates. The bold, horizontally oriented curves are Z, plotted for the study range $\theta = 400$ to 900 K in intervals of 100 K. The thin contours are u in intervals of 25 ms^{-1}; dotted contours are negative (westward, easterly). The reference gravity is $g_0 = 3.71\ \mathrm{ms}^{-2}$. The MACDA reanalysis is constrained by MGS/TES temperature retrievals at and below $\sim$40 km altitude. The dotted curve at the bottom is the silhouette of the highest surface topography; the solid curve is the zonal average, with closed circles indicating the H-grid used in the analysis.

versus B scatter plots. DDB dub this the "l'Hôpital's rule" effect, after the standard method in calculus for evaluating indeterminate forms ("0/0").

However, as just anticipated, the northern-winter profiles of Q, labeled $L_s = 270^\circ$ with a solid-line style, show flattening that exceeds any such subtlety. There is a nearly-zero potential-vorticity region that starts at the south pole, runs across the full southern hemisphere, which is in summer and which has a substantial slope of B versus latitude except in the tropical region, and then continues across the northern hemisphere to about 45° latitude. *Barnes and Haberle* (1996) first reported this $L_s \sim 270^\circ$ phenomenon for Mars, and analyzed it by adapting the zero PV (ZPV) envelope theory developed for Venus and Titan by *Allison et al.* (1994). The winter polar jet itself is associated with a large, peaked rise of Q, which is offset from the pole.

The southern-winter profiles of Q, $L_s = 90^\circ$ with a dashed-line style, do not echo the northern-winter signal, but have more in common with the equinox profiles, $L_s = 0^\circ$ and 180°. An exception is northern summer, when the $L_s = 90^\circ$ profiles drop near the north pole but the equinox profiles do not follow suit.

3.3. *Q versus B Scatter Plots*

The article's main diagnostic tool is the isentropic-coordinate Q versus B scatter plot. To help put this in context, in Fig. 6 we show typical map-view snapshots, taken at $L_s = 0^\circ$(northern spring) in MY 26, on $\theta = 500$ K. Prominent, low-wavenumber meanders, such as the one seen here in the northern mid-latitude region, are common for Mars (*Banfield et al.* 2004). Both Q and B are relatively flat in the tropical region, as mentioned above.

On Earth, the most function-like correlations occur in winter in the middle atmosphere (e.g. DDB, their Fig. 8a), so for scatter plots consider first the northern and southern winter of MY 26.

3.3.1. *Winter*

Figure 7 shows Q versus B on $\theta = 500$ K, which lies near the core of the polar jet, at the northern-winter and southern-winter solstices, $L_s = 270^\circ$ (left panel) and $L_s = 90^\circ$ (right panel). These, and the scatter plots to follow, differ in two minor aspects from those in DDB. First, we show all the data in a given hemisphere, from equator to pole, whereas DDB excluded points equatorward of $\pm 30^\circ$ latitude. Second, DDB used symbols to distinguish between mid-latitude and polar regions, but for Mars, latitude is not particularly ambiguous given the relatively simple mapping between it and B (Fig. 4). An intriguing alternative, then, is to highlight the Froude number, Fr, the ratio of wind speed to buoyancy (gravity) wave speed, which for the purposes of this article is defined to be

$$Fr \equiv \left[\frac{2K}{(NH)^2}\right]^{1/2}, \qquad (6)$$

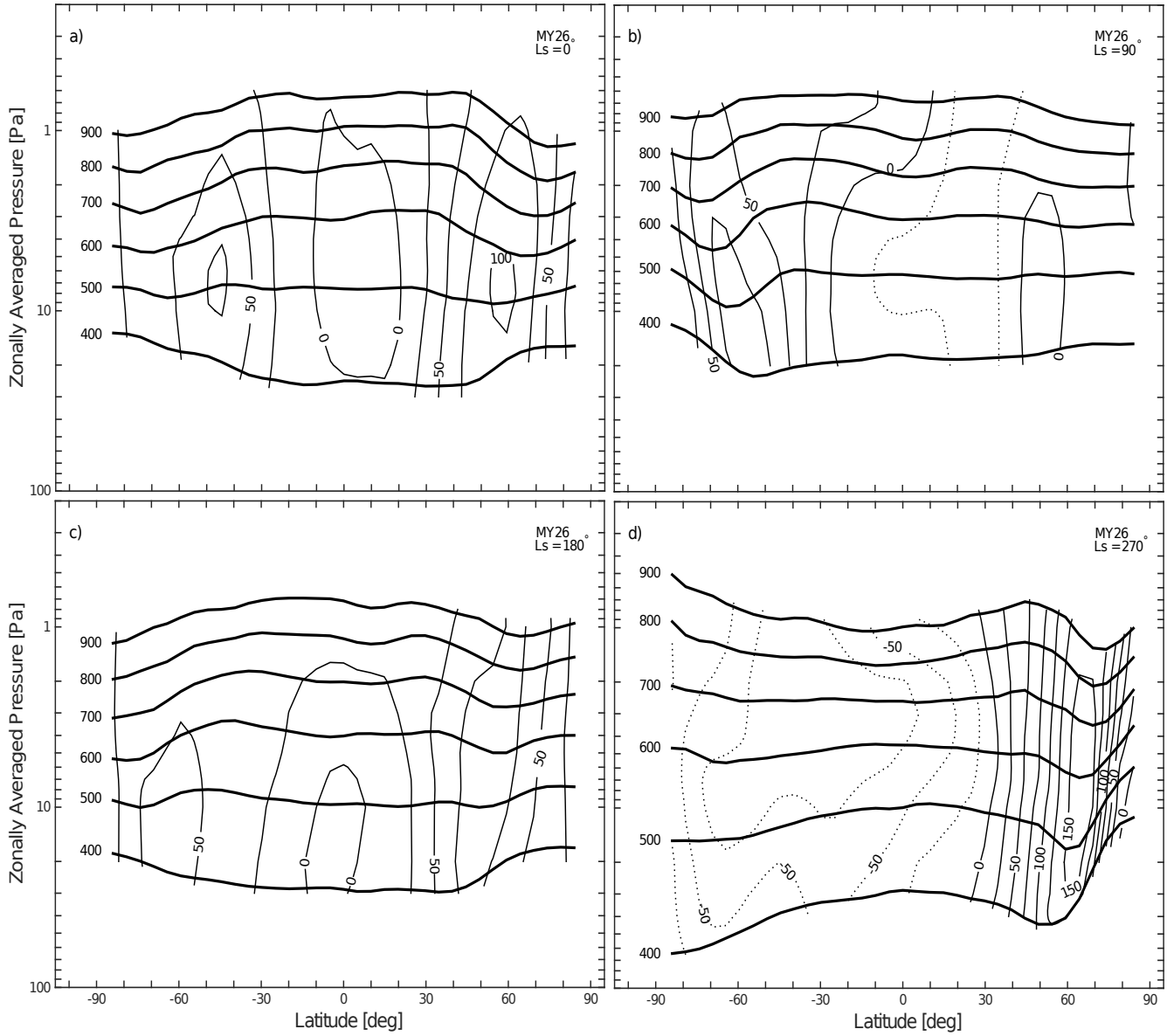

Figure 3. Similar to Fig. 2, except for pressure, p. The bottom of the plot is at 100 Pa = 1 hPa; the average surface pressure on Mars is $p_0 = 610$ Pa = 6.1 hPa.

where $(NH)^2$ is evaluated pointwise, not averaged over the region of interest. The Froude number is to buoyancy (gravity) waves what the Mach number is to sound waves, and in both cases when the value drops from above unity to below, a shock forms. In the buoyancy-wave case, this shock is called a *hydraulic jump* when it is stationary, or a *bore* when it is moving, and the terms analogous to *subsonic* and *supersonic* are *tranquil* and *shooting*. We use small-black, small-open and large-open circles to mark the three levels: $0 < Fr < 1$, $1 \leq Fr < 2$ and $2 \leq Fr$, and refer to these as tranquil, shooting and strong shooting, respectively.

Figure 7 suggests some type of uncomplicated function should capture much of the variance, just as DDB found for Earth. Perhaps the reader's first impression is the left panel looks like a woman's high-heel shoe—that was our reaction. The points that form the heel trace to the region between the north polar jet and the pole itself (Fig. 4d). A heel feature also exists in southern winter, but is less prominent (Fig. 7, right panel). In contrast, Earth tends to exhibit horizontal tips at the ends of its scatter plots, which prompted DDB to characterize the scatter plots as having the appearance of "backwards integral signs". These contrasting results are consistent with the different morphologies established for the polar vortices of each planet, for example, (see Fig. 4 of *Mitchell et al.* 2015) note that on Earth, the potential vorticity, Q, typically increases monotonically to the centre of the polar vortex, whereas on Mars, Q has a pronounced annular structure, particularly for the northern winter vortex. This annular structure is apparent in the zonally averaged Q profiles shown in Fig. 5.

A key result of this study is that in the Q versus B scatter plots for Mars, we find the heel structure is composed entirely of tranquil points, whereas in winter, most of the main arch of the shoe, which comes from the polar jet itself, is shooting to strong shooting. To our knowledge, only mesoscale atmospheric bores have been previously reported for Mars (*Rafkin et al.* 2013), and only mesoscale hydraulic jumps are known in Earth's atmosphere (apart from asteroidal impacts), and they are relatively rare (*Smith* 1988; *Rottman and Grimshaw* 2001). This juxtaposition of large tranquil and shooting regions on θ surfaces suggests the possibility of planetary-scale hydraulic jumps on Mars. We are currently investigating whether there is a causal connection between such a hydraulic jump and the heel feature and annular morphology of the martian polar vortex; however, because rotating hydraulics (*Pratt and Whitehead* 2007) is outside the scope of the present article, and the devil is in the details of 3D Lagrangian paths of air parcels, this important topic will be the subject of a future paper.

Another feature in Fig. 7 common to both winter hemispheres is a cloud of tranquil points that cluster around $Q \sim 0$ at the high-B end, the "toe" of the shoe. These points trace to the tropical

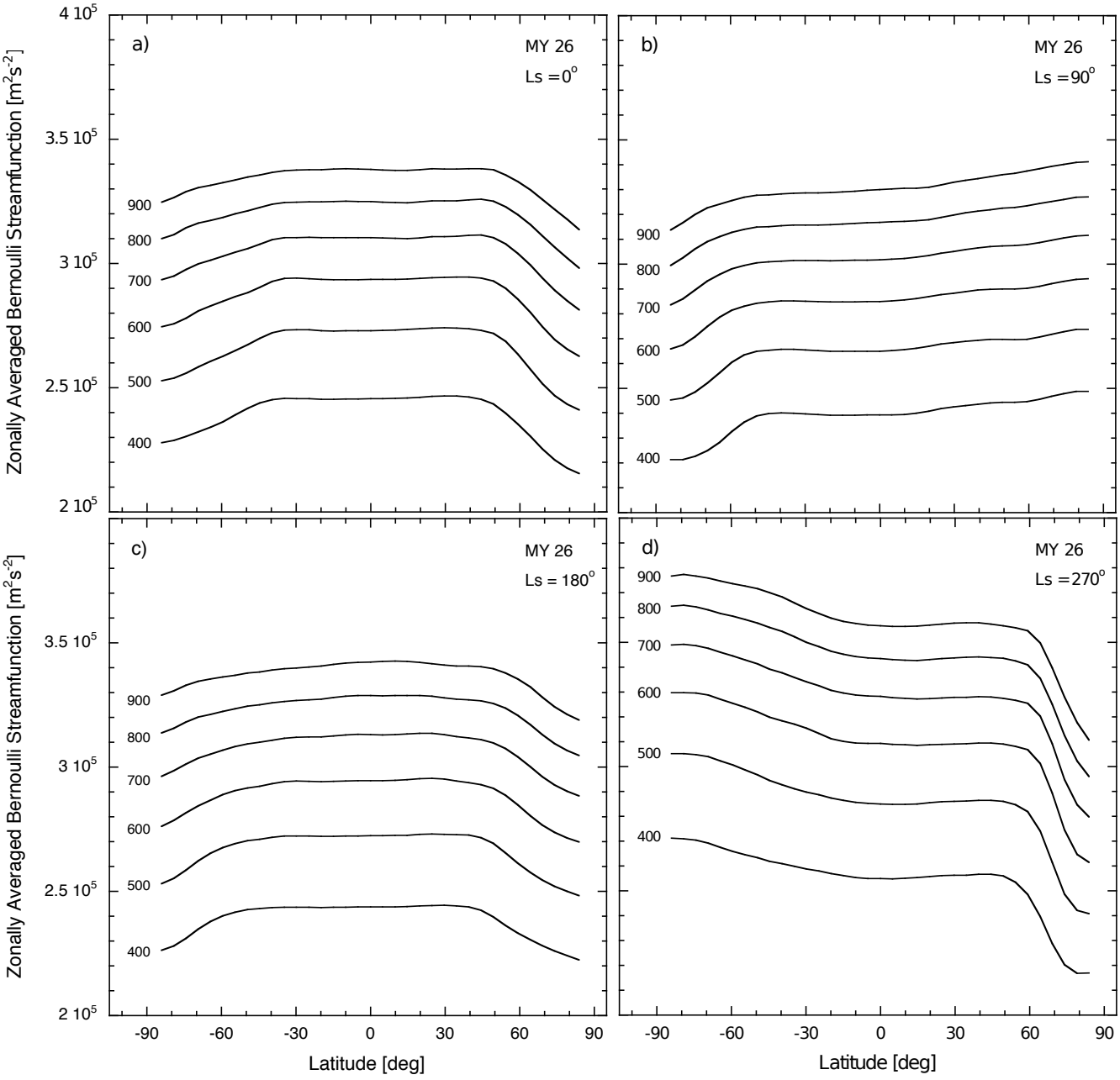

Figure 4. Similar to Fig. 2, except for Bernoulli streamfunction, $B = \phi + c_p T + K$, also known as specific total dry energy.

region. That they tend to be located on the same line as the mid-latitude trend is a manifestation of the above-mentioned l'Hôpital effect.

3.3.2. *Seasonal Variation*

Figure 8 shows northern-hemisphere snapshots at intervals of $\Delta L_s = 30^\circ$, which is one practical definition of a martian "month", on $\theta = 500$ (upper panel) and 400 K (lower panel). The correlation is tight and consistent throughout the year. The heel feature becomes small or absent from $L_s \sim 30^\circ$ to 180°, which is northern spring and summer, but is prominent throughout northern autumn and winter.

DDB found for Earth's middle atmosphere that the spread of Q, e.g. the difference between its maximum and minimum values on a given θ surface, reduces significantly in summer. It is evident in Fig. 8 that Mars shows a similar pattern. To quantify this, we calculate the standard deviation of Q on θ surfaces, σ_Q, in the mid-latitude regions for each planet, as a function of L_s. In terrestrial applications, L_s is known as the apparent ecliptic longitude; we calculate L_s for Earth by converting the start-of-month calendar times in DDB using the Great Circle Studio's online solar calculator (www.gcstudio.com/suncalc.html), which is an implementation of the astronomical algorithms described in *Meeus* (1998). Figure 9 shows a representative comparison of σ_Q between the planets. Following DDB, for Earth we use 1997 to represent a "normal" year without a SSW. The ebb and flow is quite similar between the planets. Although one might expect Earth to lag Mars because of its greater thermal inertia**, from this point of view there is no significant phase shift between the planets. Mars does exhibit a somewhat broader winter state centred around $L_s = 270^\circ$, which is consistent with the generalization by *Read et al.* (2015) that "an equinoctial state on Mars is only a relatively brief, transient phenomenon, however, as the atmosphere moves between solsticial states".

** Estimates of atmospheric radiative timescales are $\sim$ 30 days for Earth versus 1 to 2 days for Mars (*Read and Lewis* 2004), with Earth having roughly an order of magnitude greater thermal inertia, the result of its oceans, moist soil and thicker atmosphere.

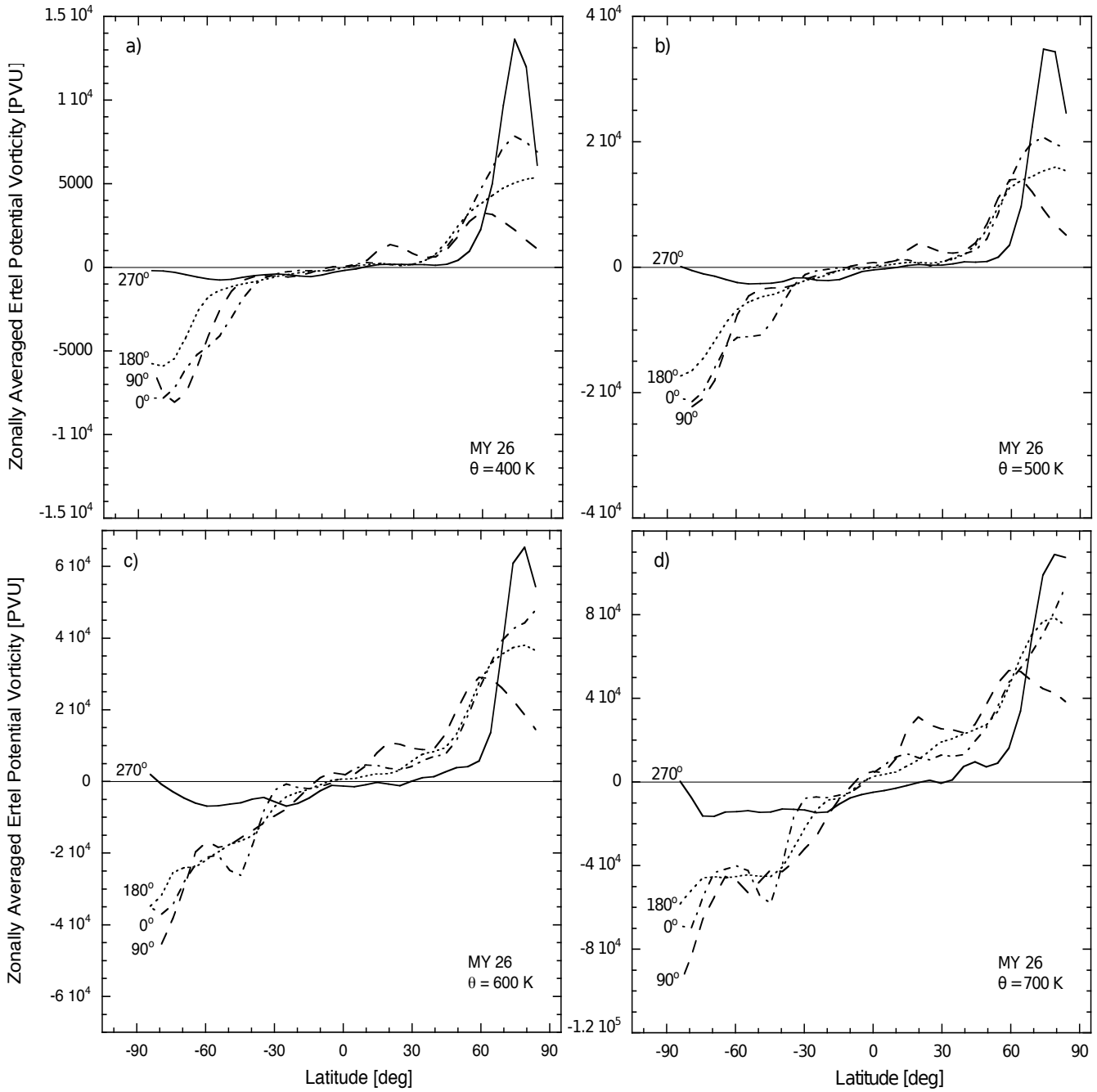

Figure 5. Potential vorticity, Q, versus latitude as a function of season. As in Fig. 2 these are snapshots from MY 26, zonally averaged in θ coordinates. The organization of the curves is transposed from the previous plots to handle the rapid increase of Q with height. The seasonal values of L_s are indicated by the labels 0° through 270°, for isentropic surfaces a) $\theta = 400$ K, b) 500 K, c) 600 K and d) 700 K.

4. Model Fits

The scatter plots in Figs. 7 and 8 exhibit good correlations between Q and B. In what follows we restrict attention to the mid-latitude component of the signal (non-heel, non-toe), which is clearly amenable to a simple regression analysis.

Notice that any single-valued, integrable function for $Q(B)$ combines with $Q = dB/d\Psi$ for steady, isentropic flow on θ surfaces to set up a triad of functions between Q, B and Ψ. Consider two such triads, starting with the exponential $Q(B)$ model (*Dowling* 2014), which DDB successfully applied to Earth's extra-tropics, expressed in terms of a correlation parameter, $\lambda_0(\theta, t)$:

$$Q \leftrightarrow B: \quad \frac{Q}{Q_0} = e^{-\lambda_0 (B - B_0)}, \tag{7a}$$

$$Q \leftrightarrow \Psi: \quad \frac{Q}{Q_0} = \left(\frac{\Psi}{\Psi_0}\right)^{-1}, \tag{7b}$$

$$\Psi \leftrightarrow B: \quad \frac{\Psi}{\Psi_0} = e^{\lambda_0 (B - B_0)}. \tag{7c}$$

In (7) the zero for Ψ is taken to be the same as the zero for Q^{-1}, and $\Psi_0 = (\lambda_0 Q_0)^{-1}$. DDB applied this to separate mid-latitude and polar regions on Earth, spanning 30° to $< 60^\circ$ latitude, and 60° to 90°, respectively, in each hemisphere. They first set B_0 to be the area-weighted average of B over each region, then applied linear regression in the form $\log|Q| = mB + b$ to obtain $\lambda_0 = -m$, with $Q_0 = \exp[b - \lambda_0 B_0]$ in the northern hemisphere and $Q_0 = -\exp[b - \lambda_0 B_0]$ in the southern hemisphere.

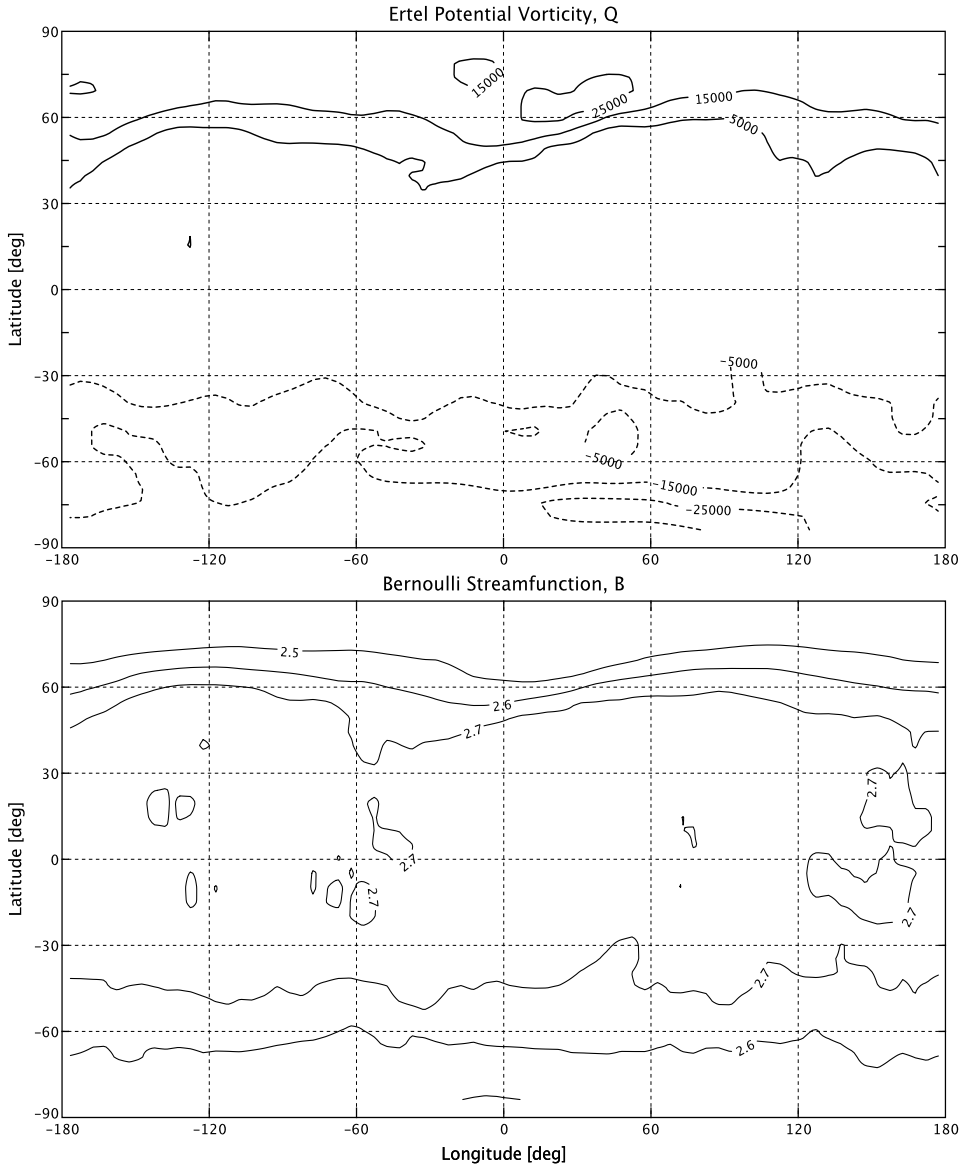

Figure 6. Map views of Q and B, on $\theta = 500\,\mathrm{K}$ at the MY 26 northern vernal equinox, $L_s = 0°$. The units for Q are $\mathrm{PVU} \equiv 10^{-6}\,\mathrm{m^2 s^{-1} K\,kg^{-1}}$ and the interval between contours is 10^4 PVU; the units for B are $10^5\,\mathrm{m^2 s^{-2}}$ and the interval is $0.1 \times 10^5\,\mathrm{m^2 s^{-2}}$. The northern-hemisphere data correspond to the leftmost scatter plot in Fig. 8a.

The Mars scatter plots tend to exhibit a slight curvature, particularly in winter, which might suggest something other than a linear $Q(B)$ model, perhaps even the exponential model just mentioned. However, the signal does not asymptote onto the $Q = 0$ line, but rather crosses it at an appreciable angle, and is fairly straight overall. Therefore, consider the linear $Q(B)$ model, written in terms of a correlation parameter, $\mu_0(\theta, t)$:

$$Q \leftrightarrow B: \quad \frac{Q}{Q_0} = 1 - \mu_0 (B - B_0)\,, \tag{8a}$$

$$Q \leftrightarrow \Psi: \quad \frac{Q}{Q_0} = e^{-\mu_0 Q_0 (\Psi - \Psi_0)}\,, \tag{8b}$$

$$\Psi \leftrightarrow B: \quad \Psi = -\frac{1}{\mu_0 Q_0} \log[1 - \mu_0 (B - B_0)] + \Psi_0\,. \tag{8c}$$

The factor Q_0 puts μ_0 on the same footing as λ_0 from the exponential model. It is interesting that in this triad, $Q(\Psi)$ is exponential rather than $Q(B)$.[††]

The linear $Q(B)$ model is viable for Mars, so long as the polar heel is treated separately. In fact it is difficult to argue against it for mid-latitude Mars in a first attempt. One can see in DDB's Fig.3b, this model is also viable for Earth in some cases, for example March and April 1997 on $\theta = 400\,\mathrm{K}$, which both exhibit impressively linear Q versus B scatter plots. Hence, in what follows we adopt (8) for mid-latitude Mars. By design, μ_0 is analogous to λ_0 in (7), as can be seen by comparing the first two terms of each Taylor series in $(B - B_0)$.

Our procedure for fitting (8a) starts by setting B_0 to be the area-weighted average of B in the region of interest, following DDB. We then apply linear regression (using the robust option in Matlab) in the form $Q = mB + b$, which yields $Q_0 = mB_0 + b$ and $\mu_0 = -m/Q_0$. The negative of the linear correlation slope itself, $-m$, is interesting in its own right; it is referred to as $\mu_0 Q_0$ below. The point of isolating μ_0 is that, like λ_0, it is proportional to the reciprocal of the analogue of the Mach number for Rossby waves (*Dowling* 2014). The point of *not* isolating μ_0 is that $\mu_0 Q_0$ is not susceptible to fluctuations in Q_0, or to future changes in the way Q_0 is defined. This arises as an issue at $L_s \sim 270°$, when the large region of nearly zero PV takes over three-quarters of the planet, dropping Q_0 and thereby raising μ_0, even as $\mu_0 Q_0$ holds steady; we solve this problem by reporting both $\mu_0 Q_0$ and μ_0.

[††] An exponential $Q(\Psi)$ is reminiscent of the sinh-Poisson equilibrium that arises in idealized two-dimensional (2D) fluid systems without rotation, where the relative vorticity evolves to become an exponential function, or a sinh function, of the most-probable non-mass-weighted streamfunction, ψ (e.g. *Montgomery et al.* 1992; *Servidio et al.* 2010).

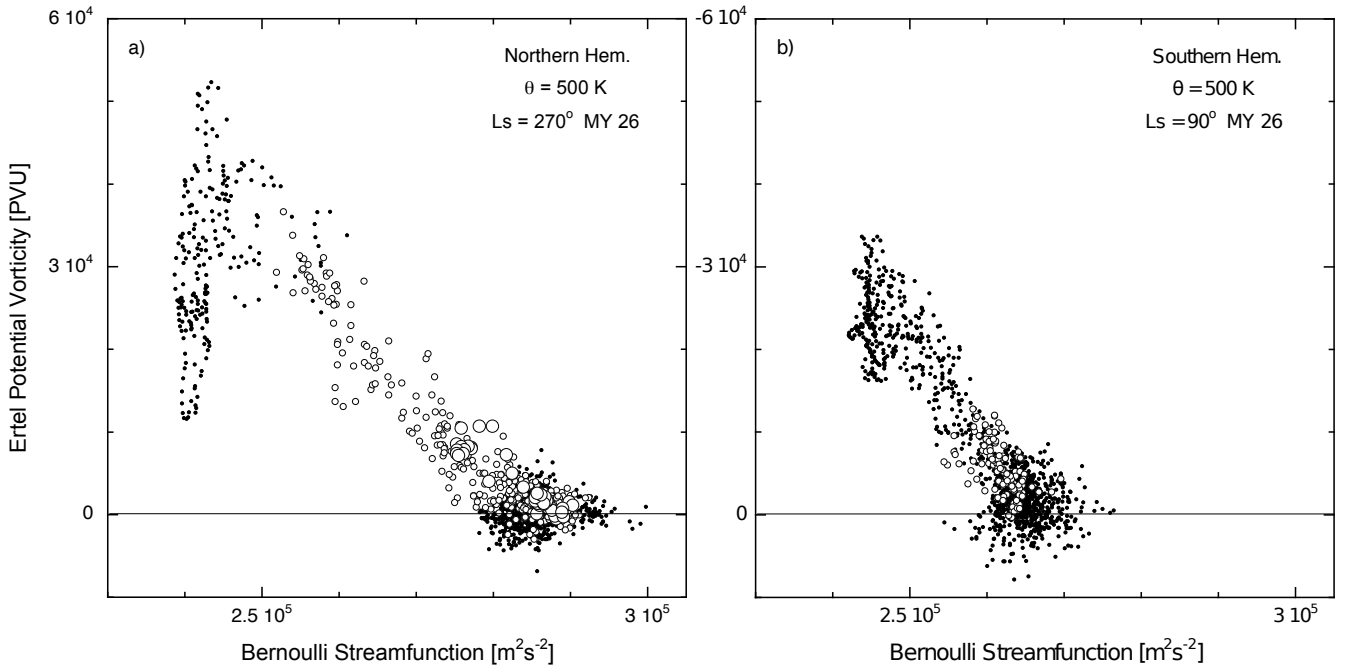

Figure 7. Scatter plots of Ertel PV versus Bernoulli streamfunction, Q versus B, on isentropic surface $\theta = 500\,\mathrm{K}$, in winter. Shown is a) the northern hemisphere during northern winter, $L_s = 270^\circ$ and b) the southern hemisphere during southern winter, $L_s = 90^\circ$, both in MY 26. Points are labeled by Froude number, Fr, with the small-black dots, small-open circles and large-open circles corresponding to $0 < \mathrm{Fr} < 1$ (tranquil), $1 \le \mathrm{Fr} < 2$ (shooting) and $2 \le \mathrm{Fr}$ (strong shooting), respectively (the latter only occur here in panel a). The ordinate in b) is reversed to facilitate comparison between the hemispheres.

4.1. Model fits for MY 26

DDB settled on two fitting regions in each hemisphere for Earth, a mid-latitude region spanning latitudes 30° up to (but not including) 60° and a polar region spanning 60° to 90°. For Mars, we want to similarly isolate the mid-latitudes, which correspond to the main body of the shoe. By trial-and-error, we find that $[45^\circ, 75^\circ]$ has too much heel, pulling the fit below the main correlation. We have settled on $[30^\circ, 70^\circ]$, which does a consistently good job of capturing the mid-latitude correlation year round.

Figures 10 and 11 show scatter plots for the northern and southern hemispheres, on $\theta = 400$, 500 and 600 K, for the four canonical season points in MY 26. Included are the corresponding best-fit lines as determined by applying (8a) to the data in $[30^\circ, 70^\circ]$ and $[-30^\circ, -70^\circ]$ latitude. The span of each best-fit line on the abscissa indicates the domain of the fitted data. These particular θ levels fall in the vicinity of the core of the winter polar jet. Higher θ levels typically lie above the $Z \sim 40\,\mathrm{km}$ altitude of the MGS/TES temperature retrievals (Fig. 2), and thus must be interpreted with caution.

Tables 1 and 2 list regression results for the northern and southern hemispheres in MY 26, including B_0, Q_0, and both versions of the correlation slopes, $\mu_0 Q_0$ and μ_0, with their standard errors. A key result is that $\mu_0 Q_0$ is remarkably steady throughout the year on Mars, changing state significantly only in summer.

In southern summer the correlation shrinks towards zero but does not change sign (the one case with a sign change in Table 2, at $\theta = 400\,\mathrm{K}$, $L_s = 270^\circ$, is not distinguishable from zero). In contrast, during northern summer, $L_s = 90^\circ$, it does change sign. Negative μ_0 or λ_0 is associated with an evanescent refractive index for Rossby-wave propagation (*Dowling* 2014). DDB found λ_0 becomes negative in both Earth's upper stratosphere and lower mesosphere, as a result of the seasonal zonal-wind reversal (*Andrews et al.* 1987). Therefore, the northern hemisphere of Mars is behaving like Earth's middle atmosphere in this respect.

Earth's troposphere shows a positive spike in correlation slope, which never changes sign and is much stronger than the signal in its middle atmosphere (Fig.1). We can therefore rule out lining up the $\theta = 400$ to 900 K region on Mars with Earth's troposphere. But, at this point, both Earth's upper stratosphere and lower mesosphere are possible analogies.

4.2. Nondimensional correlation

To refine the comparison between Mars and Earth, we nondimensionalize the signal. *Dowling* (2014) showed that scaling by a representative mean of $(NH)^2$ reduces λ_0 in Earth's middle atmosphere to order unity. DDB employ this strategy using the profile that corresponds to the U.S. Standard Atmosphere, with the result denoted $\hat{\lambda}_0 \equiv \overline{(NH)^2}\lambda_0$. Absent such a standard for Mars, we scale with the instantaneous regional mean of $(NH)^2$, calculated in the same manner as B_0. Results are listed in Tables 1 and 2. A benefit of this approach is the planet-encircling dust storm in MY 25 shows up clearly in the $[\overline{(NH)^2}]^{-1}$ time series itself (Fig. 13).

By dividing the negative of the linear-regression slope, $-m \equiv \mu_0 Q_0$, by Q_0, we isolate μ_0. The nondimensional version is $\hat{\mu}_0 \equiv \overline{(NH)^2}\mu_0$, which is analogous to $\hat{\lambda}_0$ from the exponential model. Numerical results are listed in the rightmost columns in Tables 1 and 2, and full vertical profiles for both hemispheres are plotted in Fig. 12, with different Mars years indicated by different line styles.

4.2.1. Equinoxes

Consider first the equinoxes, $L_s = 0^\circ$ (left panels) and 180° (right panels). The profiles are consistent from year to year. They start around $\hat{\mu}_0 \sim 1$ at $\theta = 400\,\mathrm{K}$, and gradually reduce with height while staying positive. This is just what $\hat{\lambda}_0$ does in Earth's lower mesosphere, from $\theta = 2000$ (the stratopause) to 3000 K (Fig. 1, shaded triangle). Significantly, nowhere else in Earth's troposphere, stratosphere or upper mesosphere does this behaviour occur.

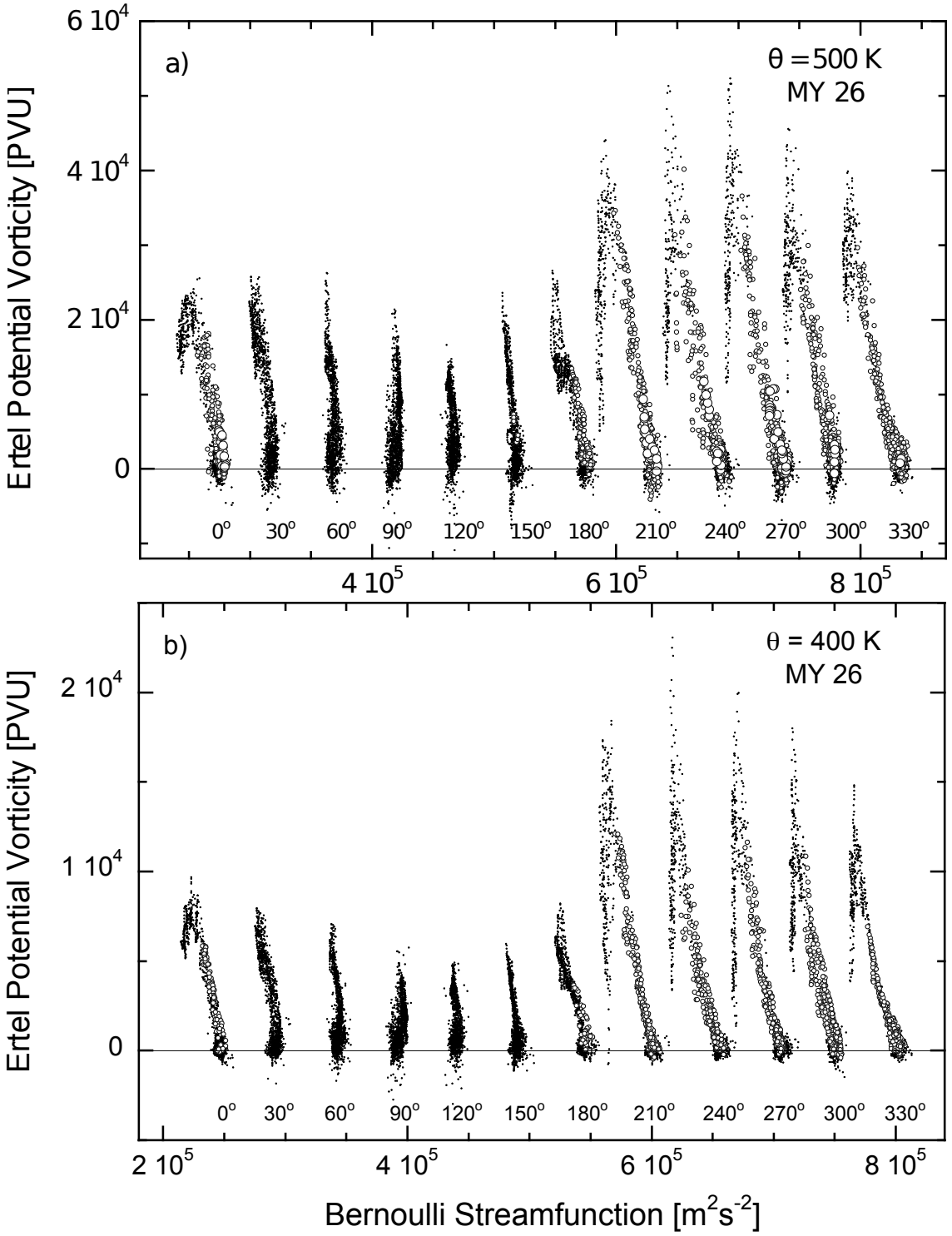

Figure 8. Seasonal evolution of Q versus B in the northern hemisphere during MY 26, on a) $\theta = 500$ K and b) $\theta = 400$ K. For clarity, B is shifted by 0.5×10^5 m^{2}s^{-2} between each time. Symbols are the same as in Fig. 7.

4.2.2. *Solstices*

Now consider $L_s = 90°$ ($L_s = 86°$ for MY 27 because the MACDA data end just before $90°$) , which is northern summer / southern winter. The northern summer profiles (upper-left panel in Fig. 12) start in $\hat{\mu}_0 \sim -0.5$ territory and reduce in absolute magnitude with height, while the southern winter profiles (lower-left panel) are not unlike equinox profiles. These results also match the behaviour of $\hat{\lambda}_0$ in Earth's lower mesosphere.

Lastly, consider $L_s = 270°$. In southern summer (lower-right panel in Fig. 12), $\hat{\mu}_0$ is essentially zero, implying homogeneous PV across the entire vertical range. The only place DDB saw something similar in Earth's extra-tropics is in the middle mesosphere, in the range $\theta = 3000$ to 4000 K. However, Earth does not have a season in which three-quarters of its latitude range exhibits homogeneous PV, so this is more likely to be a Mars-only phenomenon. The planet-encircling dust storm in MY 25 (dotted profile) is in effect at $L_s = 270°$, albeit in its decaying phase, and is not occurring elsewhere in the figure. There appears to be no sign of it in the southern (summer) hemisphere signal.

The story is different at $L_s = 270°$ in the northern (winter) hemisphere (upper-right panel in Fig. 12). As mentioned above, Q_0 is suppressed and consequently the nondimensional profiles billow into $\hat{\mu}_0 \sim 2$ territory. A change in definition of Q_0 could alleviate this problem, since it is not manifest in the $\mu_0 Q_0$ signal itself, so we do not place much weight on this billowing-out of

θ [K]	L_s [°]	B_0 [$10^5\,\mathrm{m^2 s^{-2}}$]	$\mu_0 Q_0$ [$10^{-6}\,\mathrm{s\,K\,kg^{-1}}$]	Q_0 [PVU]	μ_0 [$10^{-5}\,\mathrm{m^{-2}s^2}$]	$[\overline{(NH)^2}]^{-1}$	$\hat{\mu}_0$ [nondim]
600	0	2.914	1.48 ± 0.04	14340	10.3 ± 0.3	12.12	0.85 ± 0.03
	90	2.904	-0.80 ± 0.21	17469	-4.6 ± 1.2	12.36	-0.37 ± 0.10
	180	2.915	1.55 ± 0.03	15085	10.3 ± 0.2	11.85	0.87 ± 0.02
	270	3.071	1.54 ± 0.04	6022	25.5 ± 0.7	12.43	2.05 ± 0.06
500	0	2.701	0.75 ± 0.01	6111	12.2 ± 0.2	12.93	0.94 ± 0.02
	90	2.701	-0.10 ± 0.11	6519	-1.5 ± 1.7	14.18	-0.11 ± 0.12
	180	2.690	0.73 ± 0.01	5805	12.6 ± 0.2	12.10	1.04 ± 0.02
	270	2.833	0.67 ± 0.01	3006	22.4 ± 0.4	11.92	1.88 ± 0.03
400	0	2.418	0.286 ± 0.005	2327	12.3 ± 0.2	11.05	1.11 ± 0.02
	90	2.444	-0.160 ± 0.025	1671	-9.6 ± 1.5	14.22	-0.68 ± 0.11
	180	2.402	0.252 ± 0.004	1883	13.4 ± 0.2	11.97	1.12 ± 0.02
	270	2.520	0.278 ± 0.003	1341	20.7 ± 0.2	11.03	1.88 ± 0.02

Table 1. Northern hemisphere best-fit parameters for the linear $Q(B)$ model (8a), applied to the region spanning $[30°, 70°]$ latitude, in MY 26. The corresponding curves are plotted in Fig. 10. Also included is the square of the product of the buoyancy-wave frequency, N, and the pressure scale height, H, averaged over the region in the same manner as B_0; it is listed in reciprocal form to match the units of μ_0. The nondimensional parameter $\hat{\mu}_0 = \overline{(NH)^2}\mu_0$ is shown in the right-most column. Standard errors for the correlation parameters are indicated; 1 PVU $\equiv 10^{-6}\,\mathrm{m^2 s^{-1} K\,kg^{-1}}$.

θ [K]	L_s [°]	B_0 [$10^5\,\mathrm{m^2 s^{-2}}$]	$\mu_0 Q_0$ [$10^{-6}\,\mathrm{s\,K\,kg^{-1}}$]	Q_0 [PVU]	μ_0 [$10^{-5}\,\mathrm{m^{-2}s^2}$]	$[\overline{(NH)^2}]^{-1}$	$\hat{\mu}_0$ [nondim]
600	0	2.902	-1.27 ± 0.06	-16436	7.7 ± 0.4	11.68	0.66 ± 0.03
	90	2.825	-1.16 ± 0.09	-15963	7.3 ± 0.5	12.92	0.57 ± 0.04
	180	2.911	-0.99 ± 0.06	-16970	5.9 ± 0.3	12.66	0.47 ± 0.02
	270	3.208	-0.13 ± 0.03	-6148	2.0 ± 0.5	13.04	0.16 ± 0.04
500	0	2.692	-0.63 ± 0.02	-6972	9.1 ± 0.3	12.52	0.73 ± 0.02
	90	2.625	-1.03 ± 0.02	-5770	17.9 ± 0.4	13.82	1.30 ± 0.03
	180	2.699	-0.61 ± 0.02	-5181	11.8 ± 0.3	14.65	0.81 ± 0.02
	270	2.956	-0.04 ± 0.01	-1947	2.2 ± 0.5	13.65	0.16 ± 0.04
400	0	2.420	-0.323 ± 0.007	-2393	13.5 ± 0.3	12.32	1.10 ± 0.02
	90	2.363	-0.418 ± 0.007	-2246	18.6 ± 0.3	12.51	1.49 ± 0.02
	180	2.421	-0.272 ± 0.006	-1329	20.5 ± 0.4	14.22	1.44 ± 0.03
	270	2.627	0.002 ± 0.003	-526	-0.4 ± 0.5	13.80	-0.03 ± 0.04

Table 2. Same as in Table 1, but for the southern hemisphere. The corresponding curves are plotted in Fig. 11.

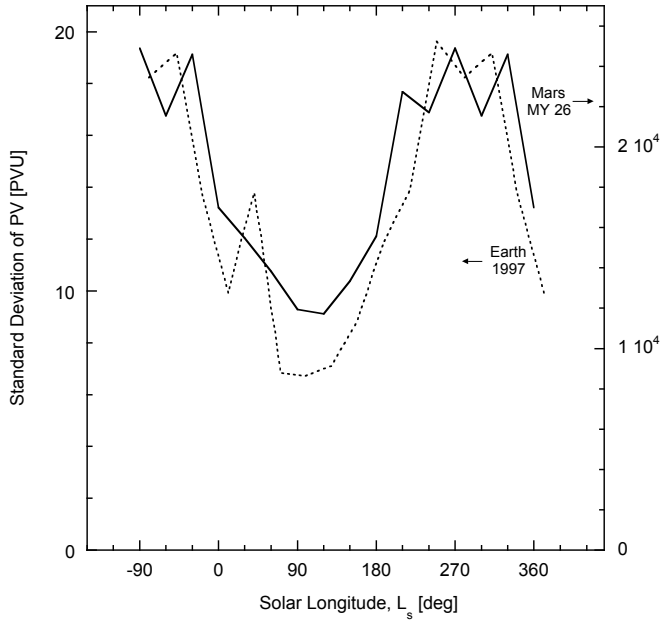

Figure 9. Sample of seasonal variation of the range of PV on isentropic surfaces for Mars and Earth. Shown is the standard deviation of Q in the northern mid-latitude region for Earth in 1997 (dotted curve, left ordinate) and for Mars in MY 26 (solid curve, right ordinate), both on their respective $\theta = 600$ K surfaces. For clarity the curves are extended by 3 months periodically.

these nondimensional profiles. Notice the dust-storm case (dotted profile) stands out from the other years in the north. The profiles eventually join up near the top of the range.

4.3. *Time series*

We now take a look at time series of $\mu_0 Q_0$ across the 3-planet-year span of the MACDA reanalysis. Figure 13 shows $\mu_0 Q_0$ versus L_s on $\theta = 550$ K, for MY 25 and 26, and Fig. 14 shows the same for the partial coverage of MY 27 and 24. The corresponding $[\overline{(NH)^2}]^{-1}$ profiles are included for reference; note $\mu_0 Q_0$ and $[\overline{(NH)^2}]^{-1}$ have different units (because of the Q_0 factor), indicated on the left and right ordinates, respectively. A result is the existence of long periods in the martian year when the vorticity-streamfunction correlation holds steady. Most of the wavering of the signal parallels the wavering in the $[\overline{(NH)^2}]^{-1}$ profile, such that $\hat{\mu}_0$ is nearly constant (apart from its susceptibility to fluctuations in Q_0).

4.3.1. *Data Irregularities*

Transient data irregularities are known to have occurred during the time period of the MACDA reanalysis; they are indicated in Fig. 13 by vertical hatching in the same manner as in Figs. 1 and 2 of *Lewis et al.* (2016). These happen when the MGS spacecraft is behind the Sun as seen from Earth, and sporadically when there is an engineering issue that affects the observing pattern or

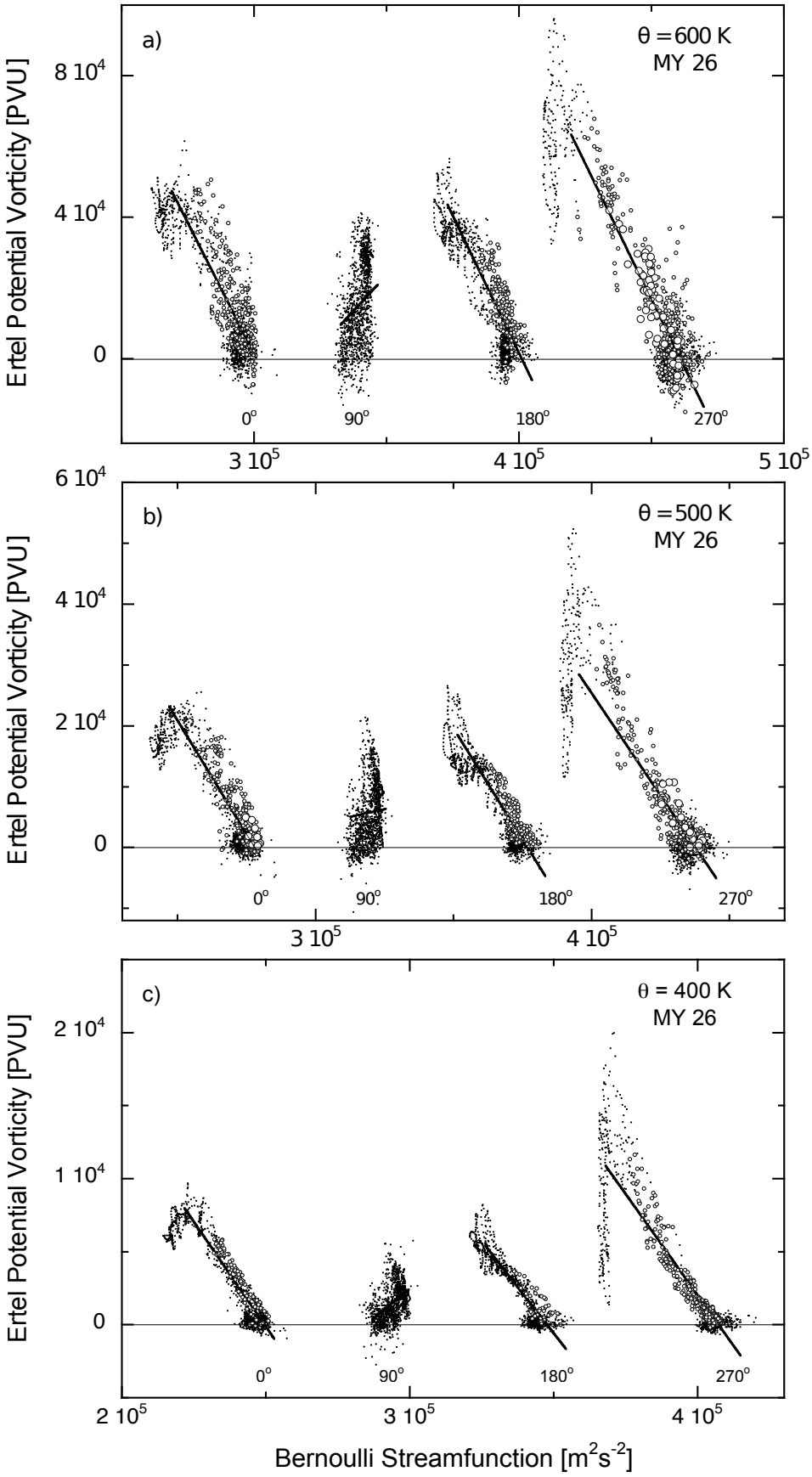

Figure 10. Northern hemisphere fits of the linear $Q(B)$ model (8a) for snapshots at the four canonical season points in MY 26, on potential-temperature levels a) $\theta = 600\,\mathrm{K}$, b) $500\,\mathrm{K}$ and c) $400\,\mathrm{K}$. Symbols are the same as in Fig. 7, with B shifted by $0.5 \times 10^5\,\mathrm{m^2 s^{-2}}$ between seasons for clarity. The regression is done on the data falling in the range $[30°, 70°]$. Solid curves show the fits plotted across the same B domain as this range. Scatter points show all the data from the northern hemisphere, including the tropical points, which cluster in a high-B, low-Q "toe". See Table 1 for best-fit parameters and standard errors.

frequency. Note that the signal in MY 26 spanning $L_s \sim 316°$ to $331°$ corresponds to a significant regional dust storm (*Mitchell et al.* 2015; *Kass et al.* 2016), as discussed below.

4.3.2. *Southern summer*

In the southern hemisphere, at $\theta = 550\,\mathrm{K}$ (Figs. 13b,d; 14b), the signal exhibits a binary state, with $\mu_0 Q_0 \approx -1 \times 10^{-6}\,\mathrm{sKkg^{-1}}$

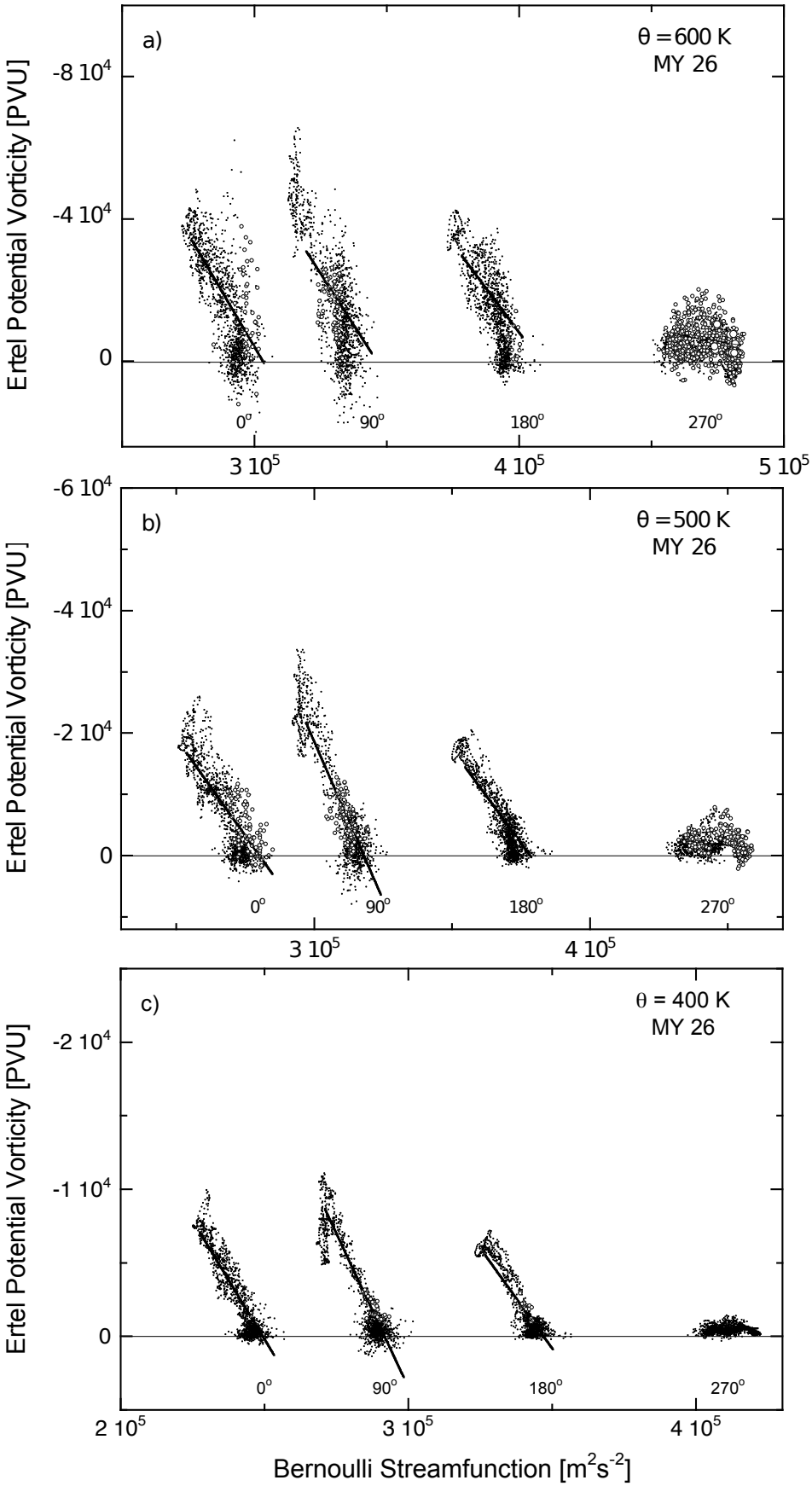

Figure 11. Same as in Fig. 10, but for the southern hemisphere. The ordinate is reversed to facilitate comparison between the hemispheres. See Table 2 for corresponding parameters.

from $L_s \approx 313 \pm 10^\circ$ through 360° (0°) to $215 \pm 20^\circ$, which then drops to $\mu_0 Q_0 \approx 0$ from $215 \pm 20^\circ$ to $313 \pm 10^\circ$. The signal is shaped like a bathtub, with an abrupt entry and a smoother exit. The entry forms nearly a right angle and is easy to pinpoint: we estimate $L_s \approx 232^\circ$, 195° and 219°, for MY 24, 25 and 26, respectively, give or take a degree. The exit is more ambiguous, but we estimate $L_s \approx 310^\circ$, 306° and 324°, respectively, give or take three degrees, such that the duration of the $\mu_0 Q_0 \approx 0$ state is roughly $\Delta L_s \approx 78^\circ$, 111° and 105°, averaging to $\Delta L_s \approx 100^\circ$ in round numbers, for the MACDA time period. The solar longitude

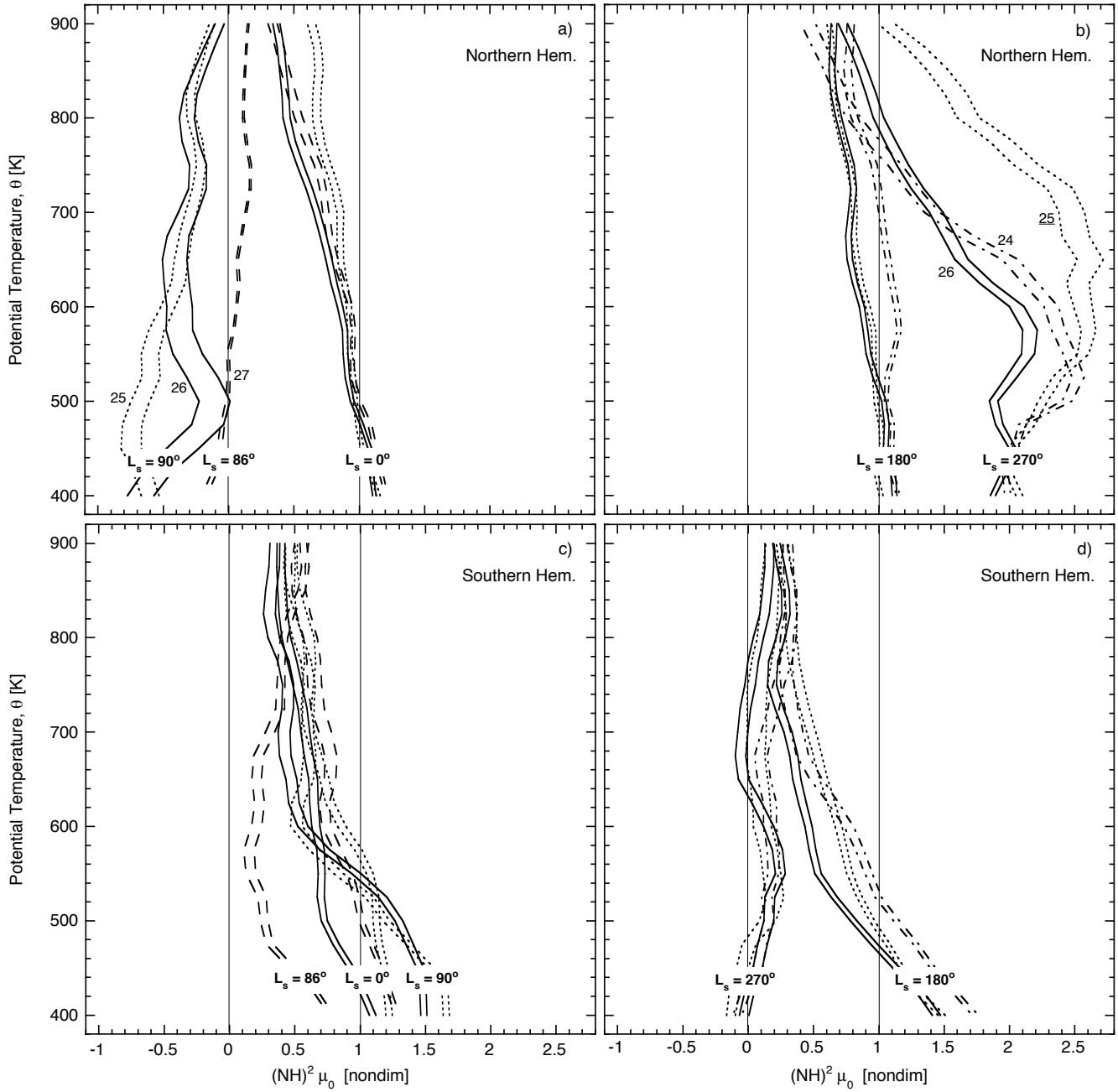

Figure 12. Profiles of nondimensional correlation parameter, $\hat{\mu}_0 = \overline{(\mathrm{NH})^2}\mu_0$, versus potential temperature, θ, at the canonical season points. The top and bottom panels correspond to the northern and southern hemispheres. The seasons naturally group together and are shown with $L_s = 0^\circ$ and 90° in the left panels and 180° and 270° in the right panels. Mars years are distinguished with dash-dot, dot, solid and dash curves for MY 24, 25, 26 and 27, respectively, shown as pairs of curves to indicate plus or minus the standard error. Note in a) and c) that $L_s = 86^\circ$ is used for MY 27 because the MACDA data stop short of 90°. The planet-encircling dust storm in MY 25 is active during $L_s = 270^\circ$ and indicated by the underlined label "25" in b). Compare with the $\hat{\lambda}_0$ signal from Earth's lower mesosphere, highlighted by the shaded triangle in Fig. 1.

interval across the top of the bathtub is more like $\Delta L_s \approx 120^\circ$, which is fully one-third of the planet's year.

It is curious how the southern-summer mode is marked by a dramatic, binary switch, yet its timing floats from year to year. The "bathtub" shape itself appears to be simply a manifestation of the strong washout of PV gradients during southern summer, whereas the dip associated with northern summer is similar to what DDB found for Earth's summers.

4.3.3. *Northern summer*

The northern summer signals in MY 26 and 27 are affected by missing data, but appear to record more than one dip (Figs. 13c; 14a), whereas MY 25 shows a single, broad, sinuous dip that is centred just after $L_s = 90^\circ$ (Fig. 13a). It is safe to say that the summer modes in the north and south on Mars would never be confused by this metric.

4.3.4. *Non-summer seasons*

Autumn, winter and spring in the southern hemisphere are relatively similar in terms of having a steady correlation signal. The story is the same in the northern hemisphere, with just the opposite sign, $\mu_0 Q_0 \approx +1 \times 10^{-6}\,\mathrm{sKkg}^{-1}$ at $\theta = 550\,\mathrm{K}$. This lack of variation outside of summer is not unlike DDB's results for Earth.

4.3.5. *Dust storms*

Mitchell et al. (2015) analyzed the regional dust storm in MY 26 that spans $L_s \sim 316^\circ$ to 331° (labeled MY 26 Storm C in *Kass et al.* 2016), which is indicated by a short, stippled bar in Fig. 13c,d. They note that this storm corresponds to a significant rise in the polar-cap temperature (averaged over latitudes 60° to 90°) measured at the bottom of the polar jet, $p = 1\,\mathrm{hPa}$, in

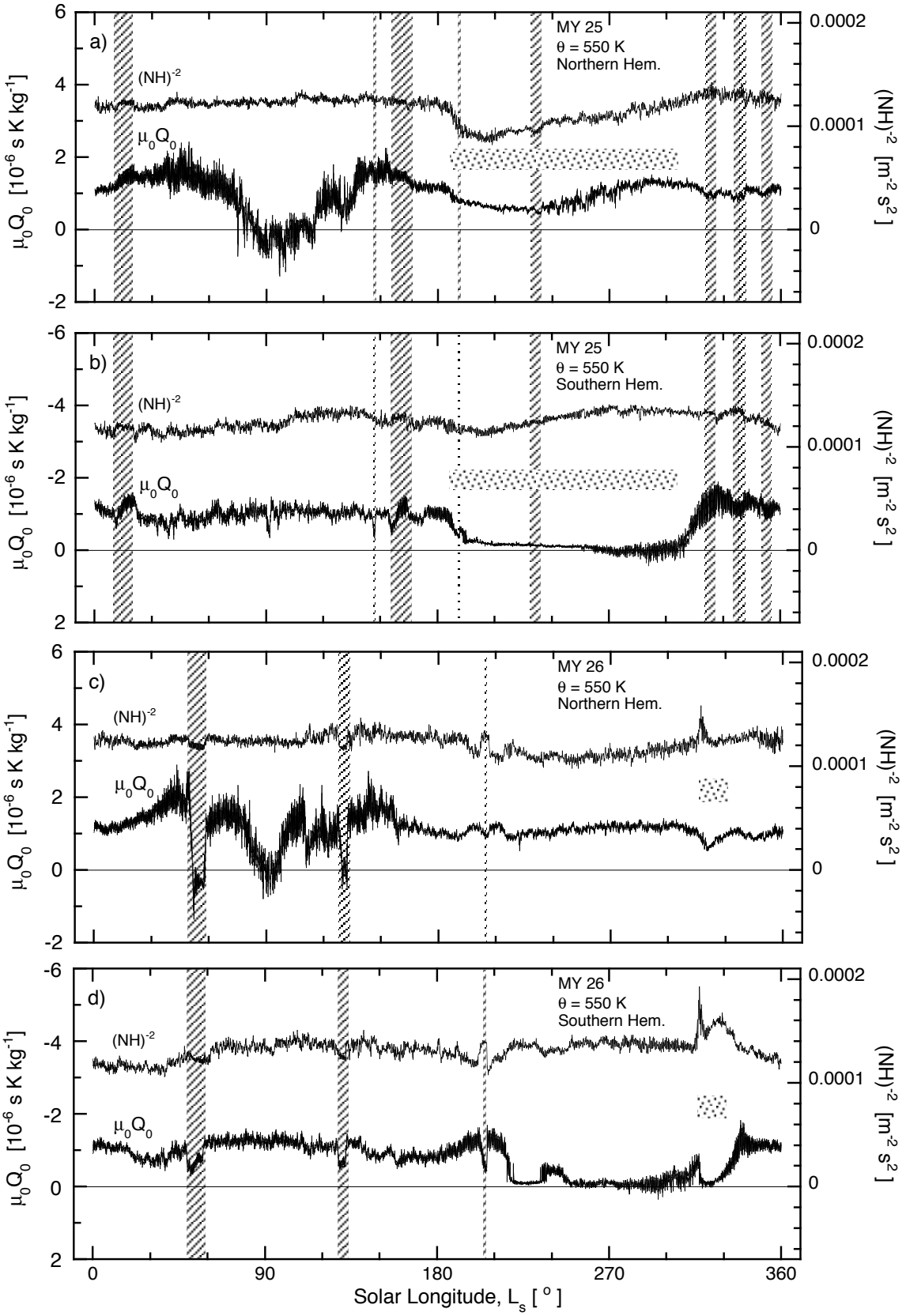

Figure 13. Time series of the correlation parameter, $\mu_0 Q_0$, and $[\overline{(NH)^2}]^{-1}$, on $\theta = 550\,\mathrm{K}$ for MY 25 in the a) northern and b) southern hemisphere, and for MY 26 in the c) northern and d) southern hemisphere. The ordinate for $[\overline{(NH)^2}]^{-1}$ is on the right. The time span of the MY 25 planet-encircling dust storm ($L_s \sim 185^\circ$ to 304°) is indicated by the horizontal stippled band in a) and b), and the time span of a significant regional dust storm in MY 26 ($L_s \sim 316^\circ$ to 331°) is likewise indicated in c) and d). Four data points per sol are plotted; vertical hatching indicates the absence of observations. The $\mu_0 Q_0$ profiles are plotted as pairs of curves to indicate plus or minus the standard error, with the corresponding (left) ordinate reversed for the southern hemisphere to facilitate comparison between the hemispheres.

both the northern and southern poles (see their Fig. 7 and the related discussion). The largest temperature rise, $\sim 10\,\mathrm{K}$, is for the north-polar cap, which they note is "comparable with minor SSW events on Earth". In the first half of the MY 26 regional dust storm, the $[\overline{(NH)^2}]^{-1}$ time series in Fig. 13c,d for both hemispheres rise sharply and then return to normal, whereas instead of a rise there is a prominent dip and linear recovery during the planet-encircling dust storm in MY 25. Contrast this with the behaviour of $\mu_0 Q_0$, which dips during both storms. Thus, in terms of the nondimensional correlation, the net result is that $\hat{\mu}_0$

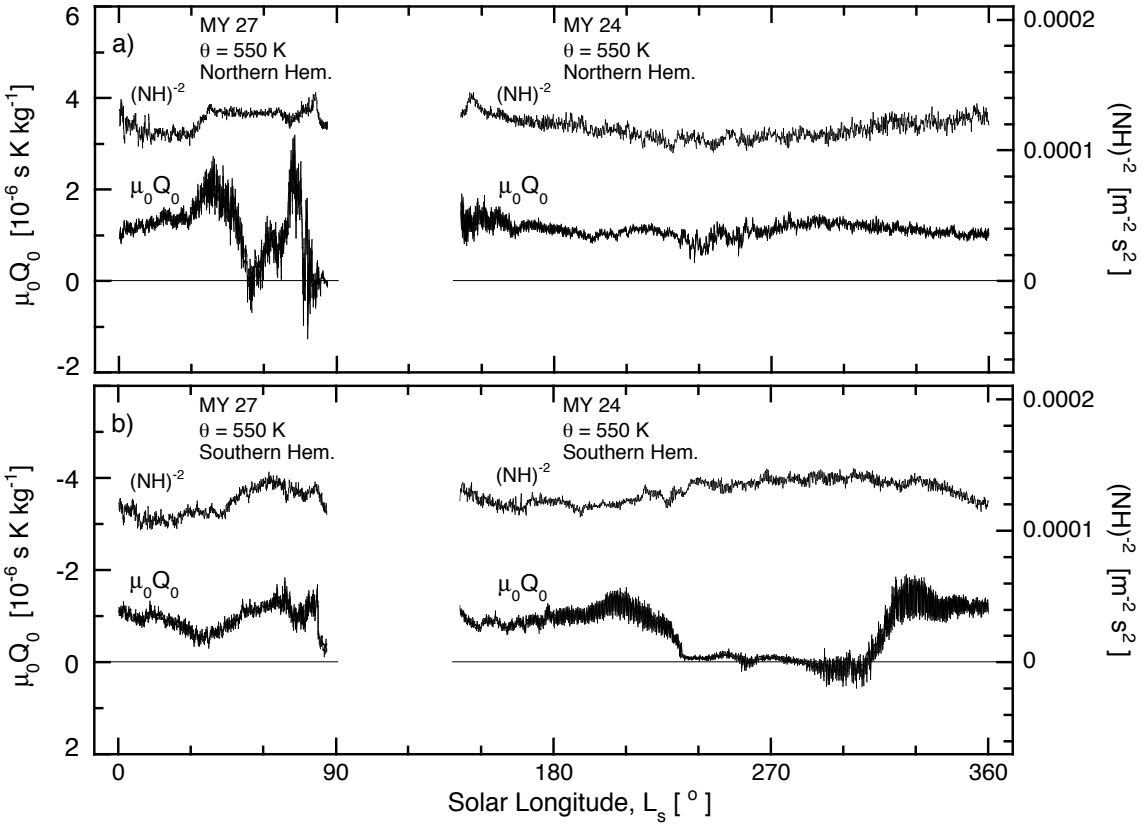

Figure 14. Same as in Fig. 13, except for the MACDA coverage of MY 27 and MY 24 (these are out of chronological order to fit on the same graph) in the a) northern and b) southern hemisphere.

drops significantly during the regional storm in MY 26, but is not strongly affected during the planet-encircling dust storm in MY 25.

DDB find $\hat{\lambda}_0$ on Earth shows a significant response to stratospheric sudden warmings (SSWs). However, the signal rises rather than falls (see their Fig. 11), so there is apparently no simple analogy with Martian dust storms, although there would appear to be sufficient diagnostic signal to warrant further investigation.

5. Conclusions

We have presented what is to our knowledge the first study of Ertel potential vorticity, Q, versus Bernoulli streamfunction, B, on potential-temperature surfaces, θ, in the atmosphere of Mars, and compared with a recent similar study for Earth (DDB). Both planets exhibit function-like correlations with some scatter, which are diagnostic of their seasonal basic states.

5.1. *Poles*

In the martian polar regions in winter, especially in northern winter, we find a nearly vertical spread of Q versus B located between the polar jet and the pole itself, which we dub the "heel" based on its appearance in the scatter plots. This signal is different from what is seen on Earth, where the polar signal tends to be flat. The MACDA data reveal regions of shooting and tranquil flow (in the sense of hydraulics) on either side of the jet, implying the possibility of a planetary-scale hydraulic jump, which would be a significant discovery if confirmed. It is known that fluid passing through a hydraulic jump does not conserve PV, so we are currently investigating the 3D Lagrangian path details, including whether or not such a jump is causing the polar heel in the scatter plots.

5.2. *Mid-latitudes*

A linear-regression analysis of Q versus B has been carried out on the mid-latitude data. On the one hand, in autumn, winter and spring, PV correlates strongly with streamfunction—it is far from homogeneous—such that it approaches a free-mode like state that is time-invariant, but which retains strong latitudinal and longitudinal gradients. This is similar to DDB's results for Earth.

On the other hand, during southern summer / northern winter, the MACDA results support the concept of homogeneous PV in the southern hemisphere and northern low latitudes, in a manner not found on Earth, but in agreement with what has already been established for Mars.

In the martian southern hemisphere, the atmosphere switches in a nearly binary fashion into and out of summer, with a signal shaped like a bathtub that spans one-third of the planet's year. The dip associated with northern summer is rounded, and multiple dips are apparent in some years.

The effects of the MY 25 planet-encircling dust storm show up nicely in $\overline{(NH)^2}$ time series, but perhaps surprisingly, are muted in the nondimensional correlation, $\hat{\mu}_0$.

Time series of the correlation signal reveal it to be keenly sensitive to input-data irregularities in the MACDA reanalysis, and hence makes a useful addition to the engineering toolbox.

5.3. *Weak nonlinear eddy-eddy interactions*

The tendency for Q to correlate strongly with streamfunction, B or Ψ, on both Earth and Mars implies relatively weak nonlinear advection of PV by the horizontal flow. This effective suppression of strongly nonlinear transport of PV is consistent with the suggestion of *Schneider* (2006, 2007) and *Schneider and Walker* (2006) that baroclinic macroturbulence in the atmosphere tends to equilibrate and self-organize into a critical state in which nonlinear eddy-eddy interactions are weak. Although reminiscent

of the earlier concept of baroclinic adjustment (e.g. *Stone* 1978), an important distinction is that such a critical state does not require or imply reduced PV gradients. With strong surface thermal gradients in the extra-tropics, the thermal stratification (and tropopause in the case of Earth) adjusts to maintain baroclinic supercriticality close to unity. This appears to hold quite well in the Earth's troposphere, consistent with what was found by DDB, and much of the time on Mars too, in stark contrast to the more classical concept of equilibration by PV mixing to remove PV gradients (e.g. *Sun and Lindzen* 1994).

5.4. *Summary*

We have found that the MACDA vorticity-streamfunction signal lines up in detail with Earth's lower mesosphere, both in terms of vertical structure and seasonal behaviour. Pressure values happen also to be in the terrestrial-mesosphere range. We conclude that the $\theta \sim 400$ to 900 K region on Mars shares significant dynamical similarities with Earth's lower mesosphere ($\theta \sim 2000$ to 3000 K). It is probably significant that these similarities hold even in the absence of an underlying stratosphere on Mars.

In closing, one serendipitous and yet intriguing result from this study is the finding that the northern-winter polar jet is associated with a transition between shooting and tranquil flow, implying a planetary-scale hydraulic jump. To our knowledge, only mesoscale bores have been previously reported for Mars. The next step is to track the 3D, oblique path-lines of parcels passing through this jump and to map out its rotating hydraulics. Questions to be addressed include determining whether previously established details such as the annular structure of the Martian polar jet are related, and to what extent the meridional-plane mass flow rate might be limited or controlled by the jump.

Acknowledgements

The authors thank Robert Haberle, Raymond Pierrehumbert and Andrew White for useful discussions, and Luca Montabone and an anonymous referee for insightful reviews that helped to improve the paper. JD acknowledges support from NSF grant AGS-1453943 and NASA grant NNX15AJ02G. SRL acknowledges support from STFC grant ST/L000776/1, UKSA grant ST/M00306X/1 and from the EU Horizon2020 project UPWARDS ref. 633127

References

Allison, M., A. D. Del Genio and W. Zhou (1994), Zero potential vorticity envelopes for the zonal-mean velocity of the Venus/Titan atmospheres, *J. Atmos. Sci.*, *51*, 694–702.

Arakawa, A. and V. R. Lamb (1977), Computational design of the basic dynamical processes of the UCLA general circulation model, *Methods Comp. Phys.*, *17*, 173–265.

Arakawa, A., and V. Lamb (1981), A potential enstrophy and energy conserving scheme for the shallow water equations, *Mon. Weather Rev.*, *109*, 18–36.

Andrews, D. G., J. R. Holton and C. B. Leovy (1987), Middle atmosphere dynamics, Academic Press.

Banfield, D., B. Conrath, P. Gierasch, R. J. Wilson and M. Smith (2004), Traveling waves in the martian atmosphere from MGS TES nadir data, *Icarus*, *170*, 365–403.

Barnes, J. R. and R. M. Haberle (1996), The martian zonal-mean circulation: angular momentum and potential vorticity structure in GCM simulations, *J. Atmos. Sci.*, *53*, 3143–3156.

Cantor, B. A. (2007), MOC observations of the 2001 Mars planet-encircling dust storm, *Icarus*, *186*, 60–96.

Charney, J. G. and P. G. Drazin (1961), Propagation of planetary-scale disturbances from the lower into the upper atmosphere, *J. Geophys. Res.*, *66*, 83–109.

Dowling, T. E. (1993), A relationship between potential vorticity and zonal wind on Jupiter, *J. Atmos. Sci.*,*50*, 14–22.

Dowling, T. E., A. S. Fischer, P. J. Gierasch, J. Harrington, R. P. LeBeau and C. M. Santori (1998). The explicit planetary isentropic-coordinate (EPIC) atmospheric model, *Icarus*, *132*, 221–238.

Dowling, T. E., M. E. Bradley, E. Colón, J. Kramer, R. P. LeBeau, G. C. H. Lee, T. I. Mattox, R. Morales-Juberías, Cs. J. Palotai, V. K. Parimi and A. P. Showman (2006), The EPIC atmospheric model with an isentropic/terrain-following hybrid vertical coordinate, *Icarus*, *182*, 259–273, doi = 10.1016/j.icarus.2006.01.003.

Dowling, T. (2014), Saturn's longitude: rise of the second branch of shear stability and fall of the first, *Int. J. Mod. Phys. D*, *23*(3), 1–32, doi:10.1142/S0218271814300067.

Du, J., T. E. Dowling and M. E. Bradley (2015), Ertel potential vorticity versus Bernoulli streamfunction in earth's extratropical atmosphere, *J. Adv. Model. Earth Syst.*, *7*, 437–458, doi:10.1002/2014MS000420.

Forget, F., F. Hourdin, R. Fournier, C. Hourdin , O. Talagrand, M. Collins, S.R. Lewis, P.L. Read and J-P. Hout (1999), Improved general circulation models of the Martian atmosphere from the surface to above 80 km, *J. Geophys. Res.*, *104*, 24155–24176.

Fritsch, F. and R. Carlson (1980), Monotone piecewise cubic interpolation, *SIAM J. Num. Anal.*, *17*, 238–246.

Gill, A. E. (1982), Atmosphere-ocean dynamics, Academic Press, Orlando.

Holton, J. R. and G. J. Hakim (2013), An introduction to dynamic meteorology, 5th ed., *Academic*.

Hoskins, B. J., M. E. McIntyre and A. W. Robertson (1985), On the use and significance of isentropic potential vorticity maps, *Q. J. Royal Meteorol. Soc.*, *111*, 877–946.

Kass, D.M., A. Kleinböhl, D.J. McCleese, J.T. Schofield and M.D. Smith (2016), Interannual similarity in the Martian atmosphere during the dust storm season, *Geophys. Res. Lett.*, *43*, 6111–6118, doi:10.1002/2016GL068978.

Konor, C. S. and A. Arakawa (1997), Design of an atmospheric model based on a generalized vertical coordinate, *Mon. Weather Rev.*, *125*, 1649–1673.

Lewis, S.R., M. Collins, P.L. Read, F. Forget, F. Hourdin, R. Fournier, C. Hourdin, O. Talagrand and J.-P. Huot (1999), A climate database for Mars, *J. Geophys. Res.*, *104(E10)*, 24177–24194.

Lewis, S. R., D. P. Mulholland, P. L. Read, L. Montabone, R. J. Wilson and M. D. Smith (2016), The solsticial pause on Mars: 1. A planetary wave reanalysis, *Icarus*, *264*, 456–464.

Marshall, J. and D. W. K. So (1990), Thermal equilibration of planetary waves, *J. Atmos. Sci.*, *47*, 963–978.

McConnochie, T. M. (2011), Planetary wave breaking and the "surf zone" in the vicinity of the martian polar vortex, In 4^{th} *International Workshop on the Mars Atmosphere: Modelling and Observations*, CNES, Paris, 8–11.

Meeus, J. (1999), Astronomical algorithms, pp. 477, 2nd Ed., Willmann-Bell.

Mitchell, D. M., L. Montabone, S. Thompson and P. L. Read (2015), Polar vortices on Earth and Mars: a comparative study of the climatology and variability from reanalysis, *Q. J. R. Meteorol. Soc.*, *141*, 550–562.

Montabone, L., K. Marsh, S. R. Lewis, P. L. Read, M. D. Smith, J. Holmes, A. Spiga, D. Lowe and A. Pamment (2014), The Mars analysis correction data assimilation (MACDA) dataset V1.0, *Geosci. Data J.*, *1*, 129–139, doi:10.1002/gdj3.13.

Montgomery, D., W. H. Matthaeus, W. T. Stribling, D. Martinez and S. Oughton (1992), Relaxation in two dimensions and the "sinh-Poisson" equation, *Phys. Fluids A*, 4, 3–6, doi:10.1063/1.858525.

Pratt, L. and J. A. Whitehead (2007), *Rotating Hydraulics*, Springer, Berlin.

Rafkin, S. C. R., J. L. Hollingsworth, M. A. Mischna, C. E. Newman and M. I. Richardson (2013), Mars: atmosphere and climate overview, Chap. 3, *Comparative Climatology of Terrestrial Planets*, Mackwell, Simon-Miller, Harder and Bullock, Eds., U. Arizona Press, 55–89.

Read, P. L., B. J. Conrath, L. N. Fletcher, P. J. Gierasch, A. A. Simon-Miller and L. C. Zuchowski (2009a), Mapping potential vorticity dynamics on Saturn: Zonal mean circulation from Cassini and Voyager data, *Planet. Space Sci.*, *57*(14), 1682–1698.

Read, P. L., T. E. Dowling and G. Schubert (2009b), Saturn's rotation period from its atmospheric planetary-wave configuration, *Nature*, *460*(7255), 608–610.

Read, P. L., P. J. Gierasch, B. J. Conrath, A. A. Simon-Miller, T. Fouchet, and Y. H. Yamazaki (2006), Mapping potential vorticity dynamics on Jupiter. I: Zonal-mean circulation from Cassini and Voyager 1 data, *Q. J. Royal Met. Soc.*, *132*(618), 1577–1603.

Read, P. L. and S. R. Lewis (2004), The Martian climate revisited: atmosphere and environment of a desert planet, *Springer-Praxis*, Chichester, UK.

Read, P. L., S. R. Lewis and D. P. Mulholland (2015), The physics of martian weather and climate: a review, *Rep. Prog. Phys.*, *78*, 125901 (54pp), doi:10.1088/0034-4885/78/12/125901.

Read, P. L., P. B. Rhines and A. A. White (1986), Geostrophic scatter diagrams and potential vorticity dynamics, *J. Atmos. Sci.*, *43*, 3226–3240.

Rottman, J. W. and R. Grimshaw (2001), Atmospheric internal solitary waves, *Environmental Stratified Flows*, Grimshaw, Ed., Kluwer, 61–88.

Schär, C. (1993), A generalization of Bernoulli's theorem, *J. Atmos. Sci.*, *50*, 1437–1443.

Schneider, T. (2006), The general circulation of the atmosphere, *Annu. Rev. Earth Planet. Sci.*, *34*, 655–688, doi:10.1146/annurev.earth.34.031405.125144.

Schneider, T. (2007), The thermal stratification of the extratropical troposphere, in *The Global Circulation of the Atmosphere: Phenomena, Theory, Challenges*, Schneider T. and A. H. Sobel, eds., Princeton Univ. Press.

Schneider, T. and C. C. Walker (2006), Self-organization of atmospheric macroturbulence into critical states of weak nonlinear eddy-eddy interactions, *J. Atmos. Sci.*, *63*, 1569–1586, doi:10.1175/JAS3699.1.

Seidelmann, P.K., B.A. Archinal, M.F. A'hearn, A. Conrad, G.J. Consolmagno, D. Hestroffer, J.L. Hilton, G.A. Krasinsky, G. Neumann, J. Oberst, P. Stooke, E.F. Tedesco, D.J. Tholen, P.C. Thomas and I.P. Williams (2007), Report of the IAU/IAG working group on cartographic coordinates and rotational elements: 2006, *Celestial Mech. Dyn. Astr.*, *98*, 155–180.

Servidio, S., M. Wan, W. H. Matthaeus and V. Carbone (2010), Local relaxation and maximum entropy in two-dimensional turbulence, *Phys. Fluids*, *22*, 125107, doi:10.1063/1.3526760.

Smith, R. K. (1988), Travelling waves and bores in the lower atmosphere: the 'Morning Glory' and related phenomena, *Earth-Science Rev.*, *25*, 267–290.

Stone, P. H. (1978), Baroclinic adjustment, *J. Atmos. Sci.*, *35*, 561–571.

Sun, D.-Z. and R. S. Lindzen (1994), A PV view of the zonal mean distribution of temperature and wind in the extratropical troposphere, *J. Atmos. Sci.*, *51*, 757–772.

Urata, R. A. and O. B. Toon (2013), A new general circulation model for Mars based on the NCAR Community Atmosphere Model, *Icarus*, *226*, 336–354, doi:10.1016/j.icarus.2013.05.017.

Vallis, G. K. (2006), Atmospheric and oceanic fluid dynamics, *Cambridge University Press*.

Wieczorek, M. A. and M. T. Zuber (2004), Thickness of the martian crust: improved constraints from geoid-to-topography ratios, *J. Geophys. Res.*, *109*, *E01009*, doi:10.1029/2003JE002153.

Woolley, H. W. (1954), Thermodynamic functions for carbon dioxide in the ideal gas state, *J. Res. Nat. Bureau Stand.*, *52*, 289–292.

White, A. A. (1990), Steady states in a turbulent atmosphere, *Meteorol. Mag.*, *119*, 1–9.

Zuber, M. (2008), Mars reconnaissance Orbiter derived gravity data, *NASA PDS*, MRO-M-RSS-5-SDP-V1.0.

Zurek, R. W., J. R. Barnes, R. M. Haberle, J .B. Pollack, J. E. Tillman and C. B. Leovy (1992), Dynamics of the atmosphere of Mars, Chap. 26 of *Mars*, Kieffer, Jakosky, Snyder and Matthews, Eds., U. Arizona Press, 934–968.

